Coseismic horizontal slip revealed by sheared clastic dikes in the Dead Sea basin

R. Weinberger[1, 2], T. Levi[1], G.I. Alsop[3], and Y. Eyal[2]

1) Geological survey of Israel, Jerusalem, Israel (rami.weinberger@gsi.gov.il)

2) Department of Geological and Environmental Sciences, Ben Gurion University of the Negev, Beer Sheva, Israel

3) Department of Geology and Petroleum Geology, School of Geosciences, University of Aberdeen, Aberdeen, UK

Abstract

Despite the hazard caused by near-surface destructive horizontal displacements during earthquakes, field evidence for coseismic slip along horizontal discontinuities is exceptionally rare, mainly due to the lack of adequate exposure and markers. However, within the seismically active Dead Sea basin, the Late Pleistocene Lisan Formation contains vertical clastic dikes at maximum depth of 15 m that are sheared laterally and thereby provide unique profiles of such horizontal displacement. In order to investigate how coseismic horizontal shearing is distributed near the surface, we document a ~1 m thick brittle shear zone, comprising up to eleven slip surfaces that can be traced for tens of meters in the Lisan Formation. Displacements along

individual slip surfaces are up to 0.6 m and the total displacement across the shear zone is up to 2.0 m. Displacement profiles and gradients indicate that the brittle shear zone formed by simple shear, and deformation was associated with slip partitioning and transfer between primary and secondary slip surfaces. Evidence for concurrent displacement along slip surfaces during a single event indicates that the brittle shear zone was formed during a coseismic event post 30 ka. We consider the mechanical effect of seismic-wave related transient stress, which when added to the initial static effective stress, may result in concurrent horizontal shear failure along detrital-rich layers in the Lisan Formation. The exceptional quality of exposures and markers enables us to document for the first time, the details of near-surface horizontal shearing, and indicates that displacement along horizontal bedding planes is a viable mechanism to absorb coseismic deformation in well-bedded near surface strata.

Introduction

Near-surface deformation could involve reactivation of preexisting joints or faults, and coseismic slip along other discontinuities such as bedding planes (Berberian, 1979; Aydin and Du, 1995; Roering et al., 1997; Berberian et al., 2000). In the case of sub-horizontal discontinuities, deformation is difficult to observe due to the typical lack of properly oriented vertical markers which would characterize such displacements. Indeed, observations of coseismic slip along horizontal discontinuities are exceptionally rare, despite the hazard caused by horizontal particle movement (i.e., destructive horizontal displacement) during near-surface seismic wave propagation.

Lake sediments deposited in seismically-active regions are prone to be deformed and reworked to form earthquake-induced horizons and structures known as seismites (Seilacher, 1969). The

late Pleistocene lacustrine Lisan Formation, widely exposed around the Dead Sea basin, exhibits several types of world-class seismites recently reviewed by Agnon (2014). In detail, the Lisan Formation comprises ~ 40 m of thin (1-5 mm) alternating white authigenic aragonite and fine dark detrital laminae, with a 1 m thick gypsum layer at the top. It provides excellent exposures of slumped horizons, which are typically less than 1 m thick. Undeformed sequences of horizontal sediments may truncate and cap each slumped unit, providing evidence that these structures are soft-sediment and slump-generated rather than related to any later tectonic deformation of a lithified sequence (Alsop and Marco, 2011, 2013, 2014). These slump sheets were postulated to be formed at the bottom of the lake by the triggering action of seismic waves (El-Isa and Mustafa, 1986; Alsop and Marco, 2011). Intraclast breccia layers ('mixed layers') were formed simultaneously with small-scale faulting and formation of micro-topography (<1 m) on the bottom of the lake (Marco and Agnon, 1995, 2005; Begin et al., 2005). Documentation of these temporal and spatial relations led Marco and Agnon (1995, 2005) to suggest a causative relationship between faulting and breccia layers. Detailed studies of breccia layers provide ample examples for fundamental characteristics of earthquakes in the Dead Sea basin, such as long-term temporal clustering, and repeated slip on the same fault planes for a limited time in the order of a few thousands of years (Marco et al., 1996; Marco and Agnon 2005). The Lisan Formation, including the slump sheets and the breccia layers, are cross-cut by hundreds of clastic dikes that have been studied in terms of fracture mechanics and magnetic-based fabric analyses (Levi et al., 2006a, b; 2008, 2009, 2011). These papers have demonstrated: (1) a physical connection between the sediment that infills dikes and clay-rich source layers in the Lisan Formation, (2) a similar mineral assemblage in both the source layers and clastic material within the dikes, and (3) a primary upward transport of clastic material within the dikes, and a

secondary horizontal transport near the source layer and below the upper gypsum layer of the Lisan Formation. Levi et al. (2006a, b) and Porat et al. (2007) concluded that the injection of clastic dikes was triggered by fluidization of the source layers during strong (M>6.5) early Holocene earthquakes along faults located at the seismically-active Dead Sea area. Levi et al. (2008) found that the emplacement of clastic dikes in the Ami'az Plain (Fig. 1) were associated with high pressure values (1-10 MPa), which probably evolved due to the passage of seismic waves through the soft lacustrine sediments. This conclusion was later supported by Shani-Kadmiel et al. (2012, 2013), who used 2D numeric simulations to suggest that the seismic waves in the Ami'az basin are amplified during an earthquake. Based on field observations and peak ground velocity calculations, Jacoby et al. (2014) proposed that the injection of clastic dikes at specific sites along the DST relates to local site effects and amplification processes.

In the present study, we utilize unique profiles of horizontal displacement expressed by laterally sheared clastic dikes within the laminated section of the Lisan Formation. These profiles provide us with a rare opportunity to investigate how horizontal shearing is distributed near the surface. We address the question as to whether the near-surface deformation is the result of gravity-driven sliding (slumping) or the product of coseismic shearing during an earthquake event. We show that the latter mechanism is more viable, and thereby expands our understanding of how deformation develops during a seismic event.

Geologic Setting

The Ami'az Plain study area is located along the southwestern margin of the Dead Sea basin, a continental depression bounded on the east by a major strike-slip fault and on the west by a series of oblique-normal faults (Fig. 1). This basin is one of several basins along the Dead Sea

Transform (DST) system. The DST system has accommodated ~105 km of sinistral displacement between the African (Sinai) and Arabian plates since the Early-Middle Miocene (Quennell, 1956; Freund, et al., 1968; Bartov, 1974; Bartov et al., 1980; Eyal et al., 1981; Garfunkel 1981) (Fig. 1a). The incision of Wadi (Nahal) Perazim in the Ami'az Plain exposes the ~40 m thick Lisan Formation, consisting mostly of alternating laminae of aragonite and fine detrital material (e.g., Begin et al., 1974). The aragonite precipitated chemically from the upper surface waters of Lake Lisan, whereas the fine detritus which contains minerals such as clay, quartz, calcite, dolomite and aragonite, was carried into the lake by annual floods. The Lisan Formation also contains several thick (>20 cm) green, clay-rich layers, which are mainly exposed in the lower and middle part of the section. The upper part of the Lisan Formation is marked by a ~1 m thick relatively competent gypsum layer. The age of the Lisan Formation, based on U–Th dating, ranges between ~70 and 14 Ka (Kaufman, 1971; Haase-Schramm et al., 2004).

The paleoseismic record from the Dead Sea basin, based on the breccia layers, reveals numerous moderate to strong earthquakes during both the late Pleistocene (e.g., Marco and Agnon, 1995; Begin et al., 2005) and also during the Holocene (Enzel et al., 2000; Ken-Tor et al., 2001; Begin et al., 2005). The strongest instrumentally recorded historical events in the Dead Sea basin are the M=6.2 Jericho earthquake of July 11, 1927, whose focal mechanism solution involved a left-lateral motion (Ben- Menahem et al., 1976; Shapira et al., 1993), and the Mw=7.2 Gulf of Aqaba earthquake of November 22, 1995 (Klinger et al., 1999; Hofstetter, 2003).

Sheared clastic dikes

112 The target section of this study is located on the Ami'az Plain, and is stratigraphically positioned
113 within the Lisan Formation about 15 m below the top of the formation. The NNE-striking ~100
114 m long outcrop is located north of the Flour cave (Fig. 1c) with an outstanding 20 m long
115 exposure at the lower part of a vertical WNW-facing cliff of Wadi Perazim. This section was
116 studied in great detail, together with several adjacent sections along Wadi Perazim. The main
117 section consists of a 113 cm thick sequence of Lisan laminae sandwiched between two green
118 clay-rich layers at the bottom and the top, which are 45 cm and 23 cm thick, respectively.

119 Tens of sheared clastic dikes cross-cut the laminae between the two green clay-rich layers (Figs.
120 2-6). The dikes are sub-vertical, up to 7 cm thick (e.g., Fig. 2a) and strike is ~WNW-ESE (Fig.
121 2c). Another minor set of sub-vertical dikes strikes ~WSW-ENE, and a few inclined dikes are
122 also observed between the two green clay-rich layers (Figs. 2a, 3). Most clastic dikes are
123 connected to the green clay-rich layer at the bottom (hereafter termed the 'lower source layer')
124 and consist of the same clay-rich detritus (Fig. 4). Inclined dikes are much more common in the
125 upper part of the studied section and are connected to the green clay-rich layer at the top
126 (hereafter termed the 'upper source layer'). Mutual cross-cutting relations are observed between
127 the sub-vertical dykes and the inclined dikes, indicating contemporaneous intrusion. A few large
128 NE- and NW- striking clastic dikes, whose source layers are located in the lower part of the
129 Lisan section, may be traced vertically for >15 m and cross-cut the entire Lisan section. These
130 prominent dikes collectively form a semi-radial and tangential dike system within the Ami'az
131 Plain (Marco et al., 2002; Levi et al., 2006a).

132 In this study, we distinguish between dike sectors and dike segments. Dike sectors are
133 disconnected sharp-edged parts of individual dikes that are displaced along slip surfaces. Dike
134 segments are continuous or discontinuous in a vertical section, but are connected at a certain

level in the third dimension. Dike segmentation in the Lisan Formation was extensively studied by Levi et al. (2009), who demonstrated that segmentation formed during dike propagation. The formation of dike sectors has not previously been documented and is the focus of the present study. The horizontal slip surfaces cut and truncate the dikes into individual 2 to 40 cm high dike sectors that can be correlated across slip surfaces based on similarities in their thickness and orientation (Figs. 2-4). The general sense of shearing as observed in the field is always top-to-the-north (or bottom-to-the-south; Figs. 2-6). The maximum apparent displacement measured along any individual slip surface is ~47 cm with an average of 15 cm.

The slip surfaces are parallel and sub-horizontal, and generally concordant with the laminae in the Lisan Formation. They dip $<1^{o}$ toward the NNE and ENE, and form a series of bedding-plane shear zones (Figs. 2, 5). The ~1 m section between the upper and lower source layers is cut by eight to eleven slip surfaces, many of which can be continuously traced for more than 20 m. A light-gray ’gouge‘ up to 10 mm thick (5 mm average) forms narrow zones along the slip surfaces (Fig. 3). The gouge consists of reworked and crushed laminae of white aragonite and dark gray detritus, the mixing of which gives rise to its light-gray color. These narrow zones, hereafter termed gouge layers, can be traced laterally for tens of meters, but infrequently can be discontinuous (Fig. 4). Their thickness may vary locally and they typically thin next to displaced dike sectors (Figs. 3, 6). Occasionally, breccia zones up to 20 mm thick accompany the gouge layers, and consist of visible clasts of laminae and rare fragments of clastic dikes.

The breccia zones are much shorter than the gouge layers, and extend laterally for several tens of cm between adjacent displaced dike sectors (Fig. 6b). Irregular breccia zones are also observed next to dike walls (Fig. 4). Thick (>50 mm) zones of intense brecciation also appear at the base of the upper source layer (Fig. 5).

158

159 Displacement profiles

160 The distributed displacement along a ~20 m long section was documented by correlating and
161 marking five prominent and continuous slip surfaces with different colored nails. For
162 convenience, these slip surfaces and associated gouge layers from bottom to top are hereafter
163 denoted by letters, 'a' to 'e', respectively (Fig. 7). Apparent displacements along slip surfaces
164 between matched pairs of adjacent dike sectors were measured by a ruler and caliper.

165 The displaced sectors of five individual dikes could be fully traced from the lower to the upper
166 source layers. Other displaced dike sectors could be only partially traced as their lower parts
167 were covered by alluvial wadi sediments. The location of each clastic dike was documented
168 along the scanline and denoted by ordered sites between 1 (southernmost site) and 29
169 (northernmost site). The upper source layer was used as a reference datum for measuring the
170 relative height of the slip surfaces. The maximum thickness of individual gouge layers was
171 measured by caliper in order to test the possibility that thicker zones of gouge are associated with
172 greater amounts of displacement. However, no such correlation was found between these two
173 variables.

174 Two sets of displaced dikes, each of which has a different orientation and amount of measured
175 (apparent) displacements along individual slip surfaces, were used to calculate the net (true)
176 displacement and its axial direction following the technique presented by Ramsay and Huber
177 (1987, p. 537). Orientations and apparent displacements of two sets of displaced dikes used for
178 the calculations are given in Figure 5. The average axial direction is 055-235º, and the true
179 displacement is 15 cm. Calculations were performed in several localities with different slip
180 surfaces and in each case remarkably similar axial directions were obtained. Consequently, the

apparent displacements were corrected into true displacements based on projection of the data into the true axial direction. Hereafter, the reported displacements are true displacements.

Vertical displacement profiles from different sites of the five fully documented dikes (incorporating displacements measured along all slip surfaces) are shown in Figure 7a, while Figure 7b displays similar profiles but accounts only for displacements measured along the prominent 'a-e' slip surfaces. All profiles (excluding site 27) show similarities, characterized by (1) a triangular or bell-like shape due to maximum displacements at the middle of the section (i.e., along the 'c' or the 'b' slip surfaces), (2) a small decrease in displacement from the uppermost 'e' slip surface to the adjacent 'd' slip surface, and (3) a decrease in displacement from the 'b' slip surface toward the lower 'a' slip surface. The profile in site 27 shows comparable displacements in the uppermost ('e' and 'd') and lowermost ('a') slip surfaces, but a dissimilar profile in between. The maximum displacement is located near the middle of the studied section, but in two profiles (25 and 29) it is located along the 'c' slip surface (~60 cm) whereas in two others (16 and 20) along the 'b' slip surface (~50 cm). The displacement profiles in Figure 7a are more irregular than those in Figure 7b, due to displacements (<40 cm) along short (a few meters long) slip surfaces, not accounted for by the continuous, (tens of meters long) slip surfaces. The 'b' slip surface terminates northward, and it was not encountered at site 29 (Fig., 7a, b).

The cumulative displacement from lower to upper source layers, for each of the five fully documented dikes, is shown in Figure 8. The obtained profiles are similar to one another and show 'S-like' shapes. The maximum and minimum cumulative displacements are 2.00 m (site 20) and 1.43 m (site 29), respectively (Fig. 8). The displacement deficit between these sites is ~0.6 m over a lateral distance of ~10 m.

Horizontal displacement profiles for each of the five labeled slip surfaces were drawn along the ~20 m scanline (Fig. 9a). The profile along the uppermost ‘e’ slip surface is quite flat with displacement values between 12 and 24 cm. The profile of the lowermost ‘a’ slip surface is somewhat similar to that of the uppermost ‘e’ slip surface, but displays slightly higher (maximum displacement 32 cm) and more variable displacement (Fig. 9a). The ‘d’ slip surface displays the lowermost displacement values among all profiles (maximum displacement 15 cm), with a constant decrease southward towards zero displacement at ~3 m (Fig. 9a). The displacement along the ‘c’ slip surface is most variable, with a maximum of 61 cm and >45 cm difference between adjacent sites (between sites 25 and 27). The profile along the ‘b’ slip surface has a triangle or a bell-like shape. The displacement has a maximum of 55 cm at ~8 m and constantly decreases northward, diminishing to zero at ~17 m.

In order to test the possibility that the displacements along secondary slip surfaces compensate and account for ’missing‘ displacements and profile fluctuation along the primary slip surfaces, we added the displacements measured along the secondary slip surfaces to that measured along the primary (‘a-e’) slip surface in two different ways: (1) the displacement along a secondary slip surface is added to the nearest primary slip surface (Fig. 9b); (2) the displacement along a secondary slip surface located between two primary slip surfaces is proportionally partitioned between them based on the relative distance to the primary slip surfaces (Fig. 9c). The modified displacement profiles show only minor changes along the ‘a’ and ‘d’ slip surfaces, and no changes were recorded along the ‘e’ slip surface (Fig. 9b, c). The apex of the modified profiles of the ‘b’ slip surface was shifted to the south (Fig. 9b, c). The modified profiles of the ‘c’ slip surface, which initially displayed large displacement deficits (e.g., site 20 at ~9 m) demonstrate, after modification, a similar magnitude of displacements as their neighboring sites (Fig. 9b, c).

227

228 AMS analysis

229 The Anisotropy of Magnetic Susceptibility (AMS) of gouge and breccia layers was measured in
230 several sites to elucidate the fabrics developed by shearing. For comparison, the AMS fabrics of
231 undeformed laminated Lisan rock, located away from the shear zones were also measured. A
232 total of 36 specimens were collected from all outcrops. The samples of site 9 include a mixture
233 of gouge and laminae in similar proportion because at this site the gouge was relatively narrow
234 and does not exceed 10 mm. In site 30, a 20 mm thick gouge and breccia layer were sampled.

235 The AMS was measured at the Geological Survey of Israel rock-magnetic laboratory using a
236 KLY-4S Kappabridge (AGICO Inc., Brno, Czech Republic). The AMS is described by its three
237 principal axes, k, k_2 and k_3, which correspond to the maximum, intermediate and minimum
238 magnetic susceptibility magnitudes, respectively. These axes with their 95% confidence ellipses
239 (Jelínek, 1978) were analyzed statistically with Anisoft42 software. Rock-magnetic properties of
240 the Lisan laminae were studied by Ron et al., (2006) and Levi et al. (2006a, b; 2014).

241 Figure 10 shows the projections of the AMS principal axes and their 95% confidence ellipses of
242 the undeformed Lisan laminae and the breccia layer in site 30. The magnetic fabric of the
243 undeformed Lisan laminae is characterized by well-grouped vertical k_3 axes in the center of
244 projection and scattered k_1 and k_2 axes along the girdle (Fig. 10a). The large and overlapping
245 95% confidence regions of k_1 and k_2 axes represents an AMS fabric typical of 'deposition'
246 (Tauxe, 1998). On the other hand, the fabric of the breccia layer is characterized by well-grouped
247 k_1, k_2 and k_3 axes with narrow 95% confidence regions (Fig. 10b). This is a distinctive 'tectonic'
248 fabric that evolves due to particle rearrangement and preferred alignment of particles during
249 shearing (Tauxe, 1998). The magnetic fabric of the gouge and laminae in site 9 (not presented)

also shows a ‘tectonic’ fabric, that is somewhat masked by the undeformed laminae that were included in the specimens during sampling.

Discussion

Brittle shear zone in the Lisan Formation

Tens of small clastic dikes emplaced in the Lisan Formation were sheared into dike sectors along bedding-plane slip surfaces. Matching of pairs of dike sectors enabled documentation of the displacement profiles of the sheared dikes in between the two source layers. The result indicates that the ~1 m section in between the two source layers has characteristics of a brittle shear zone. In ductile deformation, displacement is continuous across the shear zone, whereas in brittle shear zones, the deformation is accommodated by several discontinuities or traction surfaces (Ramsay and Huber, 1983, 1987). The present discontinuities are slip surfaces accompanied by narrow zones (<10 mm) of reworked Lisan laminae along which displacements were accommodated.

Several observations reveal that the deformation was driven mainly by simple shear displacement. First, the shear zone is characterized by displacement gradients that vary from top and bottom towards the center, with maximum displacement gradients (i.e., shear strains) in the center of the zone (Figs. 7, 8 and the section *Displacement Profiles*). Second, the sense of shear (axial direction of 055-235º) is consistent through the shear zone, but values of shear strain for individual dikes are variable (Fig. 2). Third, inclined clastic dikes which are oblique to the shear zone are displaced by different amounts, depending upon their initial angular relation to the zone (Fig. 5). Fourth, the lower and upper source layers seem to be unstrained, although the lack of markers above the upper source layer and limited exposures underneath the lower source layer

hamper the possibility of inferring that the simple shear was imposed on a thicker zone. Notably, simple shearing and the displacement of the clastic dikes could not be the result of flexural-slip folding, because the flat-laying Lisan beds are regionally almost horizontal.

Our data suggest that the displacement, in the entire brittle shear zone, occurred simultaneously during a single rather than multiple events of simple shear. First, occasional rotation of dike sectors in between two parallel slip surfaces is always with the same sense and amount of rotation. This supports simultaneous slip distribution along these surfaces, because different senses of rotation would be expected with multiple non-coaxial slip events (Fig. 5). Second, the vertical displacement profiles are typically regular and similar (Fig. 7). Third, the cumulative displacement profiles which have a characteristic S-like shape (Fig. 8) could form only if the amount of displacement along individual slip surfaces were similar and comprise the same sense of motion. Fourth, calculations of the true axial direction were performed in several localities with different slip surfaces and in each case remarkably similar results of 055-235^{o} were obtained. Fifth, narrow zones of gouge from different levels in the section show similar shear-driven magnetic fabrics with co-parallel k_1 axes. The mean direction of the k_1 axes is 063-243^{o} (Fig. 10b), which is remarkably similar to the axial direction of the true displacement (055-235^{o}). It is well known that under conditions of laminar flow, k_1 axes are commonly parallel to the transport direction (Rees and Woodall 1975; Hrouda 1982; Taira 1989; Tauxe 1998). Commonly, the magnetic fabrics of tectonic mélanges show k_1 axes, which are oriented parallel to the shear direction as estimated from measurements of P–Y intersections (Tokiwa and Yamamoto, 2012).

Termination of the brittle shear zone

295 The brittle shear zone cannot continue indefinitely and may terminate in either another
296 deformational structure (e.g., later fault) or in an undeformed Lisan section. While wadi incision
297 has not yet exposed the southern end of the shear zone, it can be traced for tens of meters
298 northward. However, the exact termination is difficult to locate due to sporadic screes, highly
299 weathered zones and inaccessible cliffs above the wadi floor. Tracing the tips of two prominent
300 slip surfaces (‘b’ and ‘d’; Fig. 9), shows that these individual slip surfaces terminate within the
301 undeformed Lisan sediments, which thus play a role in absorbing the imposed shear. The
302 cumulative displacement decreases northward (e.g., ~2 m and ~1.4 m of cumulative
303 displacement between site 20 and site 29 along the scanline; Fig. 8), suggesting that for constant
304 rate of decrease the northern end of the shear zone could be located tens of meters from the
305 studied outcrop.

306

307 *Strain partitioning and slip transfer in the brittle shear zone*

308 Most of the displacement within the shear zone is accommodated along the five primary ’a’ to
309 ‘e’ slip surfaces, which can be traced for tens of meters. The maximum shear strains (i.e.,
310 displacement gradients) were observed in the central part of the shear zone. However, the
311 displacement along slip surfaces may vary considerably, with >60 cm difference between
312 adjacent sites along the ‘c’ surface. In this part of the shear zone, the displacement was also
313 accommodated by one to four secondary slip surfaces, which extend horizontally for no more
314 than a few meters (Fig. 7a). In order to test the possibility that the displacements along secondary
315 slip surfaces compensate for ’missing‘ displacements and profile fluctuation along the primary
316 slip surfaces, we added the displacements measured along the secondary slip surfaces to that
317 measured along the primary slip surface (Fig. 9b, c). The most striking changes are seen in the

modified profiles of the ‘c’ slip surface. In this profile, sites which initially show large displacement deficits demonstrate, after modification, a similar magnitude of displacements as their neighboring sites. These results show that slip was partitioned and transferred from the primary (‘c’) to secondary slip surfaces. However, the amount of displacement is not anywhere equal along the modified profiles (i.e., compare displacements at sites 16 and 29). We attribute these variations to the conceivable bell-like shape of the displacement profiles and displacement gradients along slip surfaces. This is well supported by the displacement profiles of the ‘b’ and ‘d’ slip surfaces, in which the displacement continuously decreases toward the northern and southern peripheries (tips) of the slip surfaces, respectively. While a bell-shape profile of the displacement is commonly described for fault planes (e.g., Barnett et al., 1987; Fossen, 2010), it has seldom been described on bedding-plane slip surfaces until this study.

The formation of several secondary slip surfaces and transfer of slip from the primary to secondary slip surfaces occurs where shear strain is relatively high. Thus, formation of new secondary slip surfaces and slip transfer were enhanced by shear strain at the center of the brittle shear zone. Slip transfer between primary and secondary faults was previously reported at a much larger scale in shear zones (e.g., Eyal et al., 1986; Reheis et al., 1996; Norris and Cooper, 2001; Mouslopoulou et al., 2007). Recently, Eyal and Eyal (2015) showed that along the southwestern DST in Sinai (Egypt), kilometer-scale horizontal slip is transferred between strike slip faults via secondary strike-slip faults with measurements of displacement as accurate as ±50 m. In the present study, the measurement of meter-scale bedding-plane slip and slip transfer could be as accurate as 1 cm, based on excellent vertical markers (i.e., clastic dikes) and the size of the studied outcrop. The secondary slip surfaces are not observed splitting from the primary

slip surfaces. Hence, it is more likely that high shear strain along primary slip surfaces initiated off-plane slip on adjacent, detrital-rich layers, thereby forming secondary slip surfaces.

Origin of the brittle shear zone

The analysis of the displacement profiles and field observations suggests that the brittle shear zone was formed during a coseismic event in the Dead Sea basin. This issue is discussed below. A series of slump sheets that translate towards the NE down a very gentle (<1°) slope are identified in Wadi Perazim to the south of the Flour cave (Alsop and Marco, 2012b). Hence, slump sheets do not interfere with the brittle shear zone located north of the Flour cave. It is unlikely that the formation of the brittle shear zone was driven by surficial slumping. First, small-scale (<10 cm), individual syn-depositional folds exposed within the shear zone are cross cut by clastic dikes (Fig. 6a), indicating that sediment injection postdate syn-depositional structures. Second, the underlying source layers of the injection structures should be buried at least several meters below the surface in order to satisfy conditions of overpressure and fluidization (Levi et al., 2008). This implies that thickness of the package of Lisan laminae that should slump to cause the horizontal shear was significantly larger (>1 m) than that identified anywhere along the margins of the Dead Sea, and may therefore also be more lithified. Third, the base of the oldest slump sheet and the top of the shear zone are located ~10 m and 15 m below the present surface, respectively. It is less likely that a surficial slumping process would cause a brittle failure several meters below the surface. Fourth, if the shear zone was part of toe of the slump then NE-SW contraction is expected. However, the brittle shear zone shows NE-SW elongation (i.e, two points along individual dikes were extended along the 055-235^{o} axial direction), suggesting that it would not be located towards the contractional toe of the overlying

363 slumps. Fifth, if a package of Lisan laminae slides on top of each other downslope, the
364 displacement should increase towards the NE. However, the measured displacement in the brittle
365 shear zone actually decreases towards the NE (Fig. 8). Sixth, in one representative outcrop the
366 axial direction of the true displacement (055-235º) deviates by more than 50º from the local dip
367 of the Lisan beds. In this case, gravity-driven sliding is unlikely. Seventh, the analysis of the
368 stress conditions during horizontal shearing (see below) supports the possibility that the shearing
369 of the clastic dikes occurred after the retreat of Lake Lisan post 14 Ka, when gravity-driven
370 sliding of sediments became unlikely.

371 Begin et al. (2005) simulated the effects of strong earthquakes in Lake Lisan, and showed that
372 seiche waves might form. Seiche-induced shear at the bottom of the lake could enhance the
373 turbulent characteristics of the Lisan folds, and also lead to a component of reworking in the
374 Lisan Formation (Wetzler et al., 2010; Alsop and Marco, 2012a). However, the influence of
375 seiches or severe storm waves as triggering agents for dike shearing can be excluded because (1)
376 dikes were sheared at least several meters below the bottom of the lake and the section directly
377 above them is not convoluted (folded); (2) the vertical displacement profiles show maximum
378 shear in the center of the section, rather than the expected continuous decrease of shear from the
379 bottom of the lake downwards; and (3) the orientation of most dike sectors remains consistently
380 subvertical, indicating that no folding occurred after dike injection.

381 Late fluidization of the clay-rich source layers might induce shearing in the Lisan host rock by
382 (1) reducing the effective normal stress, and (2) increasing the shear stress (strain) along weak
383 discontinuities (i.e., detrital-rich laminae) during overpressure. Both mechanisms may result in
384 shear stress exceeding the strength of the Lisan laminae. An analog could be the failure of weak
385 bedding-planes in reservoirs by hydro-fracturing that arises due to injection-induced shearing

during production of hydrocarbons (Dusseault et al., 2001). In this scenario, at least two phases of fluidization and subsequent dike emplacement should occur. The first phase is represented by the sheared dikes and the second by a set of long straight clastic dikes that cross cut the dike sectors and the entire overlying section, indicating that they were emplaced after the formation of the brittle shear zone. The second phase of fluidization associated with the second set of long clastic dikes, might subsequently induce shear in the overburden. However, this situation is unlikely because (1) the long clastic dikes are exceptional straight and not segmented, indicating that their injection occurred after shear stress had ceased; and (2) reduction in effective stress and increase of shear stress due to fluidization would form higher shear displacement close to the source layer, contradicting the observed displacement profiles that show higher shear displacement values in the middle of the brittle shear zone (Fig. 7).

The evidence for concurrent displacement along slip surfaces suggests that the brittle shear zone was formed during a coseismic event in the Dead Sea basin. We qualitatively assume a brittle failure (i.e., seismic event) on one of the first-order faults in the western boundary fault zone of the Dead Sea basin (Fig. 11) that gives rise to seismic waves in the adjacent Lisan sediments. The seismic waves form transient stress, which moves through the rock and adding up to the initial static stress. Detrital-rich layers, mainly composed of clays, in the Lisan section have quite low shear strength (Arkin and Michaeli, 1986), and at some point the change of the initial static stress by the transient stress may lead to concurrent shear failure along several clay horizons. In favorable conditions, the transient, coseismic stress state would facilitate the growth of a brittle shear zone, in which the direction of imposed simple shear is corroborated with the direction of the body waves. Price (1968) and Price and Cosgrove (1990) considered the formation of secondary fractures next to a first-order fault by analyzing the effect of transient stress on the

adjacent rock. They preferred to invoke transient stress that was developed by the P-waves, because the velocity of S-waves is much smaller than that of P-waves. However, transient stress due to S- and surface waves might be more relevant to the formation of bedding-plane slip, because these waves are expected to cause horizontal-parallel shearing near the surface. In the following section, we quantitatively analyze the possibility that transient stress would cause failure along bedding-planes in the Ami'az basin.

Stress conditions during horizontal shearing

Based on the previous discussion, horizontal shearing of clastic dikes is considered in terms of three sequential stages: (1) static state, in which the Lisan laminae are intact, although weak zones of detrital laminae exist and are prone to failure, (2) dynamic state, in which seismic waves radiate from a source located along the Dead Sea Transform, either within the Ami'az basin or several km away from it (Jacoby et al., 2014). The seismic waves arriving at the basin are reflected back and forth, and out of the multiple possible reflection paths some are horizontal; and (3) dynamic loading, in which amplified and possibly converted surface waves result in frictional shear failure of clastic dikes along horizontal bedding planes.

The static state is considered by using the Coulomb failure criterion (Jaeger and Cook, 1979) for three geologic settings (Table 1): Setting A - the Lisan laminae are located 10 m below the bottom of the lake and are overlain by a 80 m deep water column; Setting B - the Lisan laminae are located 10 m below the bottom of the lake and are overlain by a 50 m water column; and Setting C - the Lisan laminae are located 15 m below the surface. The first two geologic settings represent 'wet conditions', which account for the fluctuation of the Lake Lisan water level (Bartov et al., 2002). The third setting represents 'dry conditions', which relates to the recession

of Lake Lisan post ~14 Ka. The shear strength of the laminated sequence of the Lisan Formation is influenced by its composition, grain size and texture. The laminated nature of the rock provides numerous potential slip surfaces, reducing the overall shear strength of the rock. An analysis of the Coulomb failure criterion of the laminated Lisan sequence in 'dry conditions' was carried out experimentally by Arkin and Michaeli (1986).

The Mohr-Coulomb failure criterion relates the failure plane shear stress, τ_s,to normal stress σn_s

$$\tau_s = C_o + \mu\sigma n_s, \quad (1)$$

where C_o is the cohesion, and μ is the coefficient of internal friction. The static stress conditions for the three geologic settings is calculated based on the values provided by Arkin and Micaheli (1986) for the laminated Lisan sequence (Table 1).

The normal stress component acting on the horizontal bedding plane is calculated based on the weight of the overburden above the bedding plane, i.e., column of lake water and weight of the Lisan rock (Table 1). The shear stress acting parallel to the bedding plane and the abscissa in Mohr's diagram is calculated based on the relation $\tau_s=\sigma n_s \cdot \nu/(1-\nu)$, where ν is Poisson's ratio of clay materials. The calculations show that settings A, B and C are on the verge of shear failure (Fig. 12).

The dynamic state is considered during an earthquake, in which significant horizontal forces are formed. Ground motion amplification in the Ami'az basin could be the result of several mechanisms such as an edge effect generated by the border faults of the basin, and different densities of rocks in the basin (mainly friable clastics) and out of it (mainly dolostones), and geometrical focusing due to basin effect (Shani-Kadmiel et al., 2012). The amplification of ground motion is formed in a special geological basin structure and lithologic section (e.g., soft

454 rocks with low seismic velocity that overlie hard rocks with a high seismic velocity). Hence, the
455 basin effect leads to amplification of ground motion and prolongs the duration of strong motions,
456 which increases seismic loading and the formation of large displacement surface waves.

457 It is unknown which type of seismic wave was associated with the shearing of the clastic dikes.
458 Yet, we can calculate the horizontal particle displacement amplitude D_a based on the relation

459 $$V_a = D_a f, \quad (2)$$

460 where V_a is the peak horizontal ground velocity and f is the shear-wave frequency. For a range of
461 V_a=0.1-0.5 m/s and f =0.3-0.9 Hz suggested by Shani-Kadmiel et al. (2012) for the Ami'az Plain,
462 the calculated D_a is comparable to the observed horizontal displacements. Hence, the observed
463 shear displacements are physically sound and may have occurred due to passing waves and their
464 amplification.

465 We consider the potential of dynamic loading associated with surface waves to form frictional
466 failure on critically stressed Lisan laminae using the Coulomb failure criterion. We limit our
467 analysis to initially static stress fields and surface-wave dynamic stress acting on horizontal
468 surfaces. The analysis was formulated by Hill (2008, 2012), who calculated the dynamic stress
469 pulse of surface waves that triggered frictional failure. For the present implication of Hill's
470 approach, the dynamic triggering is based on the premise (a) the laminated Lisan sequence was
471 at least locally, in a state of near incipient failure and (b) a component of the dynamic stress
472 field, $\delta\tau(t)$, temporarily nudges the total stress acting on an optimally oriented surface greatly
473 beyond the Coulomb failure threshold. In the present case study, the optimally oriented and
474 mechanically weak zone is horizontal detrital-rich Lisan laminae, with the interfaces between
475 these and aragonite laminae probably representing the most susceptible surface for shear failure.

476 Dynamic triggering implies that transient stress carried by seismic waves may lead to shear
477 failure. The range of dynamic stress triggering greatly exceeds that of static stress triggering.
478 Generally, the surface wave stress amplitude falls in the range of 0.5-1 MPa. Dynamic stress, τ_d,
479 of shear waves can be estimated by (e.g., Hill, 2012 a, b):

480 $$\tau_d = GV_a/V_s, \quad (4)$$

481 where G is the shear modulus of the rock and V_s is the shear wave velocity. We calculated the
482 dynamic stress based on representative values of V_a=0.1-0.5 m/s and f=0.3-0.9 Hz (Shani-
483 Kadmiel et al., 2012, V_s=100 m/s (e.g., Aboye et al., 2011; Bessason and Erlingsson, 2011) and
484 G=100 MPa (Levi et al., 2008 and references therein) and obtained a dynamic stress of $\tau_d \approx$ 0.1-
485 0.5 MPa.

486 During the passage of surface waves, the local stress field fluctuates in both amplitude and
487 orientation. Hill (2012) defines a time-dependent dynamic change in Coulomb failure stress
488 δCFF(t) that acts during the passage of seismic waves:

489 $$\delta CFF(\gamma, t) = \delta\tau_d(\gamma, t) - \mu\delta\sigma n_d(\gamma, t), \quad (5)$$

490 with $\tau_d(\gamma, t)$ and $\sigma n_d(\gamma, t)$ being the time-dependent shear stress and normal stress, respectively,
491 imposed on the mechanically weak plane by seismic waves and γ is the incident angle from the
492 source.

493 The particle motion is depth-dependent. Thus, the amplitude of both $\tau_d(\gamma, t)$ and $\sigma n_d(\gamma, t)$
494 changes with depth. Nevertheless, in the present case study, we impose σn_d = 0.1 and 0.5 MPa,
495 assuming that the stress amplitude of the surface waves are at least equal to that of the body
496 waves.

For several wave incidence angles between 0 and 360º and imposing θ=60º (the angle between σn_d and σ_1), the values of δCFF (γ, t) for settings A-C were calculated (Fig. 12). Figure 13 demonstrates the distribution of δCFF values calculated for setting A (Polygon #1), B (Polygon #2) and C (Polygon #3) for $0<\gamma<360^{o}$ and $0.1\leq\tau_d\leq0.5$ MPa. A larger polygon with positive values of δCFF is more likely interconnected to dynamic triggering.

Polygon #1 is relatively small and narrow with negative δCFF values. Polygon #2 is larger than Polygon #1 and one-third of it has positive δCFF values. Polygon #3 is the largest and almost entirely consists of positive values. This indicates that almost all of the observed displacements presented by Polygon #3 can be explained by dynamic triggering and frictional failure. Notably, setting C ('dry conditions') has a greater tendency to fail under a range of dynamic stress than settings A and B ('wet conditions'). This tendency is hold even for the case of τ_d>0.5 MPa (and V_a>0.5 m/s). Hence, the above calculations seem to support the possibility that the shearing of the clastic dikes occurred after the retreat of Lake Lisan post 14 Ka. We conclude that dynamic triggering provides a viable mechanism to explain shearing along bedding planes and formation of coseismic deformation.

Age of the brittle shear zone

The age of the Lisan formation, ranges between ~70 and 14 Ka (Kaufman, 1971; Haase-Schramm et al., 2004). Based on the stratigraphic position of the Lisan section, the formation of the shear zone postdated ~30 Ka. The age of the long and undeformed dikes and their injection, based on optically stimulated luminescence (OSL) dating of the clastic-dike material ranges between 15 and 7 Ka, (Porat et al., 2007). These ages provide an approximate time interval for the emplacement of the present studied clastic dikes, which are older than 7 Ka (youngest age of

long and undeformed dikes) and younger than 30 Ka (depositional age of the Lisan Formation). Hence, it is likely that the coseismic event that initiated the formation of the brittle shear zone occurred during the Holocene, predating 7 Ka. The Holocene Ze'elim Formation exhibits plentiful seismites (e.g., Bookman et al., 2004), indicating that late Pleistocene to Holocene earthquakes have repeatedly affected the lake deposits on the western margin of the Dead Sea basin. Hence, we cannot reject the possibility that other shear zones in different locations and levels of the Lisan Formation exist, but so far remain undiscovered.

Conclusions

The well-laminated lacustrine Lisan Formation in the Ami'az basin contains numerous horizontal displaced dike sectors that form a prominent ~1 m thick brittle shear zone ~15 meters below the present surface (i.e., top of the Lisan Formation). The brittle shear zone comprises up to eleven slip surfaces, five of which are primary discontinuities that can be traced for tens of meters. Displacements along individual slip surfaces are up to 0.6 m and the total displacement across the shear zone is up to 2.0 m. Field observations and displacement profiles and gradients indicate that the brittle shear zone formed by simple shear. Deformation was associated with slip partitioning and transfer between primary and secondary slip surfaces, mainly at the center of the zone. Evidence for concurrent displacement along slip surfaces suggests that the brittle shear zone was formed during a coseismic event in the Dead Sea basin. It is likely that failure during a DST-related earthquake results in body or surface waves in the adjacent Lisan rock. Subsequently, these waves form transient stress, which moves through the rock and is added to the initial static effective stress. Detrital-rich layers in the section of the Lisan Formation have low shear strength. Therefore, a change of the initial static stress by the transient stress might

lead to concurrent horizontal shear failure along several of these layers during the late Pleistocene to Holocene. The exceptional quality of exposures and markers helps to document the effect of near-surface horizontal shearing due to a single coseismic event. Displacement profiles show the shearing distribution along horizontal slip surfaces, and provide indications for slip transfer and partitioning due to a strong earthquake. We suggest that displacement along horizontal bedding planes is a viable mechanism to absorb coseismic deformation in well-bedded strata near the surface. However, such deformation is typically difficult to measure in paleo- and recent earthquakes due to a lack of adequate exposures and markers.

Acknowledgements

This study was supported by the Israel Science Foundation (ISF grant No. 1245/11).We thank the Associate Editor, E. Tavarnelli, and two anonymous reviewers for their careful and constructive reviews of the manuscript.

References

Aboye, S., Andrus, R. D., Ravichandran, N., Bhuiyan, A. and Harman, N., 2011, Site factors for estimating peak ground acceleration in Charleston, South Carolina, based on V_S30. *Proc., 4th IASPEI/IAEE International Symposium: Effects of Surface Geology on Seismic Motion*, University of California Santa Barbara, CA.

Agnon, A., 2014, Pre-Instrumental Earthquakes Along the Dead Sea Rift, *in* Garfunkel, Z., Ben-Avraham, Z., and Kagan, E.J. eds., Dead Sea Transform Fault System: Reviews, Springer Netherlands, p. 207–261.

Alsop, G.I., and Marco, S., 2011, Soft-sediment deformation within seismogenic slumps of the Dead Sea Basin: Journal of Structural Geology, v. 33, no. 4, p. 433–457, doi: 10.1016/j.jsg.2011.02.003.

568 Alsop, G.I., and Marco, S., 2012a, Tsunami and seiche-triggered deformation within offshore
569 sediments: Sedimentary Geology, v. 261-262, p. 90–107, doi:
570 10.1016/j.sedgeo.2012.03.013.

571 Alsop, G.I., Marco, S. 2012b. A large-scale radial pattern of seismogenic slumping towards the
572 Dead Sea Basin. Journal of the Geological Society, v. 169, p. 99-110.

573 Alsop, G.I., and Marco, S., 2013, Seismogenic slump folds formed by gravity-driven tectonics
574 down a negligible subaqueous slope: Tectonophysics, v. 605, p. 48–69, doi:
575 10.1016/j.tecto.2013.04.004.

576 Alsop, G.I., and Marco, S., 2014, Fold and fabric relationships in temporally and spatially
577 evolving slump systems: A multi-cell flow model: Journal of Structural Geology, v. 63, p.
578 27–49, doi: 10.1016/j.jsg.2014.02.007.

579 Arkin, Y., and Michaeli, L., 1986, The significance of shear strength in the deformation of
580 laminated sediments in the Dead Sea area: Isr. J. Earth Sci., v. 35, p. 61–72.

581 Aydin, A., and Du, Y.J., 1995, Surface rupture at a fault bend - the 28-June-1992 Landers,
582 California, earthquake: Bulletin of the Seismological Society of America, v. 85, no. 1, p.
583 111–128.

584 Barnett, J.A., Mortimer, J., Rippon, J.H., Walsh, J.J., and Watterson, J., 1987, Displacement
585 geometry in the volume containing a single normal fault: AAPG Bull., v. 71, p. 925–937.

586 Bartov, Y., 1974, Structural and paleogeographical study of the Central Sinai faults and domes:
587 Ph.D. Thesis, Hebrew University, Jerusalem 143 p. (in Hebrew, English abstract).

588 Bartov, Y., Steinitz, G., Eyal, M., and Eyal, Y., 1980, Sinistral movement along the Gulf of
589 Aqaba - its age and relation to the opening of the Red Sea: Nature, v. 285, p. 220–221.

590 Bartov, Y., Stein, M., Enzel, Y., Agnon, A., and Reches, Z., 2002, Lake levels and sequence
591 stratigraphy of Lake Lisan, the late Pleistocene precursor of the Dead Sea: Quaternary
592 Research, v. 57, p. 9–21.

593 Begin, Z.B., Ehrlich, A., and Nathan, Y., 1974, Lake Lisan, the Pleistocene precursor of the
594 Dead Sea: Geol. Surv. Isr. Bull., v. 63, p. 30.

595 Begin, B.Z., Steinberg, D.M., Ichinose, G.A., and Marco, S., 2005, A 40,000 years unchanging
596 of the seismic regime in the Dead Sea rift: Geology, v. 33, no. 4, p. 257–260.

597 Ben-Menahem, A., Nur, A., and Vered, M., 1976, Tectonics, seismicity and structure of the
598 Afro-Eurasian junction- the breaking of an incoherent plate: Physics of the Earth and
599 Planetary Interiors, v. 12, p. 1–50.

Bessason, B., and Erlingsson, S., 2011, Shear wave velocity in surface sediments. Jökull, v. 61, p. 51-64.

Berberian, M., 1979, Earthquake faulting and bending thrust associated with the Tabas-e-Golashan (Iran) earthquake of September 16, 1978: Bull. Seis. Soc. Am., v. 69, no. 6, p. 1861–1887.

Berberian, M., Jackson, J.A., Qorashi, M., Talebian, M., Khatib, M., and Priestley, K., 2000, The 1994 Sefidabeh earthquakes in eastern Iran : blind thrusting and bedding-plane slip on a growing anticline , and active tectonics of the Sistan suture zone:.

Beroza, G.C., 1991, Near-source modeling of the Loma Prieta earthquake: evidence for heterogeneous slip and implications for earthquake hazard: Bulletin of the Seismological Society of America, v. 81, no. 5, p. 1603–1621.

Bookman, R., Enzel, Y., Agnon, A., and Stein, M., 2004, Late Holocene lake levels of the Dead Sea: Bull. Geol. Soc. Am., v. 116, p. 555–571.

Dusseault, M.B., Bruno, M.S., and Barrera, J., 2001, Casing shear: causes, cases, cures: SPE J. Reservoir Eng, v. 16, p. 98–107.

El-Isa, Z.H., and Mustafa, H., 1986, Earthquake deformations in the Lisan deposits and seismotectonic implications: Geophys. J. R. Astron. Soc., v. 86, p. 413–424.

Enzel, Y., Kadan, G., and Eyal, Y., 2000, Holocene earthquakes inferred from a fan-delta sequence in the Dead Sea graben: Quaternary Research, v. 53, no. 1, p. 34–48.

Eyal, M., Eyal, Y., Bartov, Y., and Steinitz, G., 1981, The tectonic development of the western margin of the Gulf of Elat (Aqaba) rift: Tectonophysics, v. 80, p. 39–66.

Eyal, Y., Eyal, M., Bartov, Y., Steinitz, G., and Folkman, Y., 1986, The origin of the Bir Zereir rhomb-shaped graben, eastern Sinai: Tectonics, v. 5, p. 267–277.

Eyal, Y., and Eyal, M., 2015, Nature of slip transfer between strike-slip faults: The Eastern Sinai (Egypt) shear zone, Dead Sea Transform: Journal of Structural Geology, v. 76, p. 52–60, doi: 10.1016/j.jsg.2015.03.014.

Fossen, H., 2010, *Structural geology*. Cambridge University Press, 463 p.

Freund, R., Zak, I., and Garfunkel, Z., 1968, Age and rate of the sinistral movement along the Dead Sea Rift: Nature, v. 220, p. 253–255.

Garfunkel, Z., 1981, Internal structure of the Dead Sea leaky transform (rift) in relation to plate kinematics: Tectonophysics, v. 80, p. 81–108.

631 Haase-Schramm, A., Goldstein, S.L., and Stein, M., 2004, U-Th dating of Lake Lisan (late
632 Pleistocene Dead Sea) aragonite and implications for glacial East Mediterranean climate
633 change: Geochimica Et Cosmochimica Acta, v. 68, no. 5, p. 985–1005.

634 Hrouda, F., 1982, Magnetic-anisotropy of rocks and its application in geology and geophysics,
635 *Geophys. Surv.*, v. 5, p. 37–82.

636 Hill, D.P., 2008, Dynamic Stresses, Coulomb Failure, and Remote Triggering: Bulletin of the
637 Seismological Society of America, v. 98, no. 1, p. 66–92, doi: 10.1785/0120070049.

638 Hill, D.P., 2012, Dynamic Stresses, Coulomb Failure, and Remote Triggering--Corrected:
639 Bulletin of the Seismological Society of America, v. 102, no. 6, p. 2313–2336, doi:
640 10.1785/0120120085.

641 Hofstetter, A., 2003, Seismic observations of the 22/11/1995 Gulf of Aqaba earthquake
642 sequence: Tectonophysics, v. 369, no. 1-2, p. 21–36.

643 Jacoby, Y., Weinberger, R., Levi, T., and Marco, S., 2014, Clastic dikes in the Dead Sea basin as
644 indicators of local site amplification: Natural Hazards, v. 75, no. 2, p. 1649–1676, doi:
645 10.1007/s11069-014-1392-0.

646 Jaeger, J.C., and Cook, N.G.W., 1979, Fundamentals of Rock Mechanics: Chapman and Hall,
647 London, 593 p.

648 Jelinek, V., 1978, Statistical processing of anisotropy of magnetic susceptibility measured on
649 group of specimen, *Stud. Geophys. Geod.*, v. 22, p.50–62.

650 Kaufman, A., 1971, U series dating of Dead Sea basin carbonates: Geochimica Et Cosmochimica
651 Acta, v. 35, p. 1269–1281.

652 Ken-Tor, R., Agnon, A., Enzel, Y., Marco, S., Negendank, J.F.W., and Stein, M., 2001, High-
653 resolution geological record of historic earthquakes in the Dead Sea basin: J. Geophys. Res.,
654 v. 106, no. B2, p. 2221–2234.Klinger Y., Rivera L., Haessler H., Maurin J.C., 1999. Active
655 faulting in the Gulf of Aqaba: New knowledge from the Mw 7.3 earthquake of 22
656 November 1995, Bull. Seism. Soc. Am., v. 89, p.1025–1036.

657 Levi, T., Weinberger, R., Aifa, T., Eyal, Y., and Marco, S., 2006a, Earthquake-induced clastic
658 dikes detected by anisotropy of magnetic susceptibility: Geology, v. 34, p. 69–72.

659 Levi, T., Weinberger, R., Aïfa, T., Eyal, Y., and Marco, S., 2006b, Injection mechanism of clay-
660 rich sediments into dikes during earthquakes: Geochemistry, Geophysics, Geosystems, v. 7,
661 no. 12, doi: 10.1029/2006GC001410.

662 Levi, T., Weinberger, R., and Eyal, Y., 2009, Decay of dynamic fracturing based on three-
663 dimensional measurements of clastic-dike geometry: Journal of Structural Geology, v. 31,
664 no. 8, p. 831–841, doi: 10.1016/j.jsg.2009.06.002.

Levi, T., Weinberger, R., Eyal, Y., Lyakhovsky, V. and Hefez, E., 2008, Velocities and driving pressures of clay-rich sediments injected into clastic dikes during earthquakes.Geophys. J. Int. 175**,** 1095–1107.

Levi, T., Weinberger, R., and Marco, S., 2014, Magnetic fabrics induced by dynamic faulting reveal damage zone sizes in soft rocks, Dead Sea basin. Geophys. J. Int. v. 199, p. 1214-1229.

Marco, S., and Agnon, A., 1995, Prehistoric earthquake deformations near Masada, Dead Sea graben: Geology, v. 23, no. 8, p. 695–698.

Marco, S., and Agnon, A., 2005, High-resolution stratigraphy reveals repeated earthquake faulting in the Masada Fault Zone, Dead Sea Transform: Tectonophysics, v. 408, no. 1-4, p. 101–112.

Marco, S., Stein, M., Agnon, A., and Ron, H., 1996, Long term earthquake clustering: a 50,000 year paleoseismic record in the Dead Sea Graben: J. Geophys. Res., v. 101, no. B3, p. 6179–6192.

Marco, S., Weinberger, R., and Agnon, A., 2002, Radial clastic dykes formed by a salt diapir in the Dead Sea Rift, Israel: Terra Nova, v. 14, p. 288–294.

Mouslopoulou, V., Nicol, A., Little, T. a., and Walsh, J.J., 2007, Displacement transfer between intersecting regional strike-slip and extensional fault systems: Journal of Structural Geology, v. 29, no. 1, p. 100–116, doi: 10.1016/j.jsg.2006.08.002.

Norris, R.J., and Cooper, A.F., 2001, Late Quaternary slip rates and slip partitioning on the Alpine Fault, New Zealand: Journal of Structural Geology, v. 23, no. 2000.

Porat, N., Levi, T., and Weinberger, R., 2007, Possible resetting of quartz OSL signals during earthquakes—Evidence from late Pleistocene injection dikes, Dead Sea basin, Israel: Quaternary Geochronology, v. 2, no. 1-4, p. 272–277, doi: 10.1016/j.quageo.2006.05.021.

Price, N., 1968, A dynamic mechanism for the development of second order faults, *in* Baer, A.J. and Norris, D.K. eds., Proc. Conf. on Research in Tectonics, Geol. Surv. Can. GSC paper, p. 68–72.

Price, N., and Cosgrove, J., 1990, Analysis of geological structures: Cambridge University Press.

Quennell, A.M., 1956, Tectonics of the Dead Sea rift, *in* Congreso Geologico Internacional, 20th sesion, Asociacion de Servicios Geologicos Africanos, Mexico City, p. 385–405.

Ramsay, J.G., and Huber, M.I., 1983, Techniques of Modern Structural Geology: Volume I: Folds and Fractures: Academic Press, 307 p.

Ramsay, J.G., and Huber, M.I., 1987, Techniques of Modern Structural Geology: Volume II: Folds and Fractures: Academic Press, 393 p.

Rees, A. I., and Woodall, W.A., 1975, The magnetic fabric of some laboratory-deposited sediments. Earth and Planetary Science Letters, v. 25 no. 2, p. 121-130.

Reheis, M.C., and Survey, U.S.G., 1996, Kinematics of the Eastern California shear zone : Evidence for slip transfer from Owens and Saline Valley fault zones to Fish Lake Valley fault zone: Geology, v. 24, no. 4, p. 339–342.

Roering, J., Cooke, L., and Pollard, D., 1997, Why blind thrust faults do not propagate to the Earth's surface: Numerical modeling of coseismic deformation associated with thrust-related anticlines: Journal of Geophysical Research, v. 102, p. 11901–11912.

Ron, H., Nowaczyk, N.R., Frank, U., Marco, S. and McWilliams, M.O., 2006, Magnetic properties of Lake Lisan and Holocene Dead Sea sediments and the fidelity of chemical and detrital remanent magnetization in *GSA Book New Frontiers in Dead Sea Paleoenvironmental Research*, p. 171–182, eds Enzel, Y., Agnon, A. and Stein, M., GSA Special Paper 401.

Seilacher, A., 1969, Fault-graded beds interpreted as seismites: Sedimentology, v. 13, p. 155–159.

Shani-Kadmiel, S., Tsesarsky, M., Louie, J.N., and Gvirtzman, Z., 2012, Simulation of Seismic-Wave Propagation through Geometrically Complex Basins: The Dead Sea Basin: Bulletin of the Seismological Society of America, v. 102, no. 4, p. 1729–1739, doi: 10.1785/0120110254.

Shapira, A., Avni, R., and Nur, A., 1993, A new estimate for the epicenter of the Jericho earthquake of 11 July 1927: Isr. J. Earth Sci., v. 42, no. 2, p. 93–96.

Sneh, A., Weinberger, R., 2014, Major Structures of Israel and Environs, Geological Survey of Israel, scale 1: 500,000.

Taira, A., 1989, Magnetic fabrics and depositional processes, in *Sedimentary Facies in the Active Plate Margin*, p. 43–47, eds Taira, A. and Masuda, F. Terrapub, Tokyo.

Tauxe, L., 1998, *Paleomagnetic Principles and Practice*: Kluwer Academic Publishers, 299 p.

Tokiwa, T., Yamamoto, Y., 2012. Relationship between magnetic fabrics and shear directions in m_elange within the Miyama formation, Shomanto accretionary complex, Japan. Tectonophysics v. 568-569, p. 53-64.

Wetzler, N., Marco, S., and Heifetz, E., 2010, Quantitative analysis of seismogenic shear-induced turbulence in lake sediments: Geology, v. 38, no. 4, p. 303–306, doi: doi: 10.1130/G30685.1.

Figure Captions

Figure 1: Location maps. (a) general plate tectonic configuration of the sinistral Dead Sea Transform (DST), (b) regional setting of the Dead Sea basin. Solid lines – major faults at the surface; dashed lines – major faults in the subsurface (after Sneh and Weinberger, 2014). The Ami'az Plain study area is marked by a rectangle. (c) enlargement of the study area. Outcrops are located next to the Flour cave in Wadi Perazim. Traces of several first-order clastic dikes are marked by solid lines (after Marco et al., 2002).

Figure 2: (a) Photograph of a sheared (top-to-the-north) clastic dike (site 16). Numbers mark nine individual dike sectors that are displaced along horizontal slip surfaces that are sub-parallel to the bedding. Locations of underlying and overlying source layers are indicated. (b) Schematic diagram illustrating a clastic dike displaced by bedding parallel slip surfaces between two source layers. (c) Stereoplot of poles to dike orientations (N=24) measured from sites along a ~50 m scanline, north of the Flour cave (see Fig. 1c for location). The majority of dikes trend WNW-ESE, whereas a minority strike WSW-ENE. Contour intervals are 5% per 1% area.

Figure 3: Inclined clastic dike displaced along a horizontal slip surface (top-to-the-north), associated with a bedding-parallel, gray gouge layer. The gouge thins beneath the northern dike sector. Inset: general view showing an array of three dike sectors displaced along two slip surfaces. Coin diameter is 25 mm and position of main photograph is boxed.

Figure 4: Photo (mirrored) and drawing of a stock-like structure in the lower source layer, which connects upward to a sub-vertical clastic dike. The upper part of the dike, not seen in the figure, is displaced (top-to-the-north) along a prominent and continuous slip surface associated with a several mm thick gray gouge layer. Several gouge layers marking discontinuous slip surfaces, where offset of the dike is less than the width of segment, do not cross the dike (e.g. displacement of the lowermost segment is less than the width of the dike). A zone of brecciation adjacent to the dike wall is also indicated.

Figure 5: Photo (mirrored) and interpretative line drawing of a displaced clastic dike (top-to-the-north), and five parallel, sub-horizontal slip surfaces that are marked by several mm thick gouge layers. Two sets of clastic dikes with different orientation and thickness are marked with light (dip to ENE) and heavy (dip to WSW) gray. They are displaced along individual slip surfaces and serve to calculate the true axial direction and net displacement (see text). A dike sector at the center of the photo is rotated relative to other sectors of the same dike, in between two adjacent slip surfaces, suggesting simultaneous shear along adjacent slip surfaces. Orientations of dike sectors are labeled (dip/dip direction), indicating that displacements are apparent in this view. Younger NE-dipping normal faults displace both laminae, clastic dikes and gouge layers.

Figure 6: (a) Two dike sectors displaced across three sub-horizontal gouge layers marking slip surfaces. An angular enclave of folded Lisan laminae is clearly visible within a dike sector. The sharp contacts between the host rock and the enclave indicate that the dike was emplaced when the Lisan host rock was brittle and already folded. Dike smearing along the uppermost slip surface is indicated. The gouge thins underneath both segments. Coin diameter is 25 mm; (b)

775 Two displaced dike sectors. Lisan breccia with a fine gouge along the upper surface marks a sub-
776 horizontal shear zone. Brecciation is most prominent between the two dike sectors. Coin
777 diameter is 25 mm.

778

779 Figure 7: Vertical displacement profiles of five displaced clastic dikes offset along five major
780 slip surfaces between the lower and upper source layers that serve as reference levels. (a) All true
781 displacements, including those along short slip surfaces are shown. Five prominent slip surfaces
782 extending for tens of meters are denoted by ‘a’ (lowermost surface), ’b’, ’c’, ‘d’ and ‘e’
783 (uppermost surface). (b) Only true displacements computed along prominent slip surfaces
784 (labeled by letters) are shown. Locations of sites along the N-S scanline transect are indicated.

785

786 Figure 8: Cumulative (total) displacement profiles computed between the lower and upper source
787 layers for five displaced clastic dikes. The top of the lower source layer serves as a reference
788 level. Locations of sites along the N-S scanline transect are shown at the bottom. The cumulative
789 displacement decreases northward and therefore the displacement gradient (total displacement
790 divided by height) between the two source layers decreases from 1.75 (site 20) to 1.25 (site 29).
791 Notably, the displacement gradients are much higher in the middle part of the section.

792

793 Figure 9: (a) Displacement profiles along the five prominent slip surfaces noted in the text. Sites
794 13 and 29 are located at the southernmost and the northernmost ends of the scanline,
795 respectively. (b) Modified displacement profiles in which displacements along short ’unlabelled‘
796 slip surfaces are added to the nearest labeled‘ slip surface. (c) Modified displacement profile in

797 which the displacement along a secondary slip surface located between two primary slip surfaces
798 is proportionally partitioned between them based on the relative distance to the primary slip
799 surfaces. Arrows indicate the relative change in displacement. The ‘e’ slip surface has not been
800 changed. In site 20, secondary slip surfaces accommodate two thirds of the cumulative
801 displacement at the zone next to the ‘c’ slip surface. In site 25, only one secondary slip surface
802 exists (Fig. 7) and accommodates one third of the cumulative displacement next to the ‘c’ slip
803 surface. In site 27, the displacement deficit along the ‘c’ slip surface is the maximum.

804

805 Figure 10: Lower-hemisphere, equal-area projections of AMS principal axes and their 95%
806 confidence ellipses of (a) undeformed Lisan laminae, (b) ~20 mm thick gouge and breccia
807 sampled from site 30. k_1. k_2, k_3 axes are marked by squares, triangles and circles, respectively.

808

809 Figure 11: Schematic sketch illustrating the orientation and kinematics of displaced clastic dikes
810 in the Ami’az basin adjacent to the Western border fault zone and the Sedom diapir in the
811 southwestern margin of the Dead Sea basin. The thickness of the Lisan Formation is highly
812 exaggerated. Notably, the maximum displacement of the sheared dike is located near the middle
813 of the Lisan shear zone.

814

815 Figure 12: Mohr’s diagram for static and dynamic loading. Static states of stress for geologic
816 setting A, B and C are illustrated by circles. The solid line represents the Coulomb failure
817 criterion for the Lisan Formation and the dashed line the failure criterion for the static stress state
818 of geologic setting A (see Table 1). The effect of the dynamic loading is illustrated for geologic

819 settings A and C based on Hill's (2008) method. The perturbation of the dynamic stress, τ_d, σ_{nd}
820 and 2γ are imposed on the two static circles. The two horizontal dashed lines show the δCFF(t)
821 values of geologic setting A; positive values are above the failure criterion for static condition
822 and negative values are below the line.

823

824 Figure 13: Range of possible δCFF(t) values versus range of $0 < \gamma < 360^{o}$ calculated using Hill's
825 (2008, 2012) method. The three polygons mark the δCFF(t) values with, τ_d=0.5 MPa and τ_d=0.13
826 MPa. Polygons #1 #2 and #3 represent geologic settings A, B and C, respectively.

Figure

Click here to download Figure
Figures_sheared_dikes_22_12_2015 BW.pdf

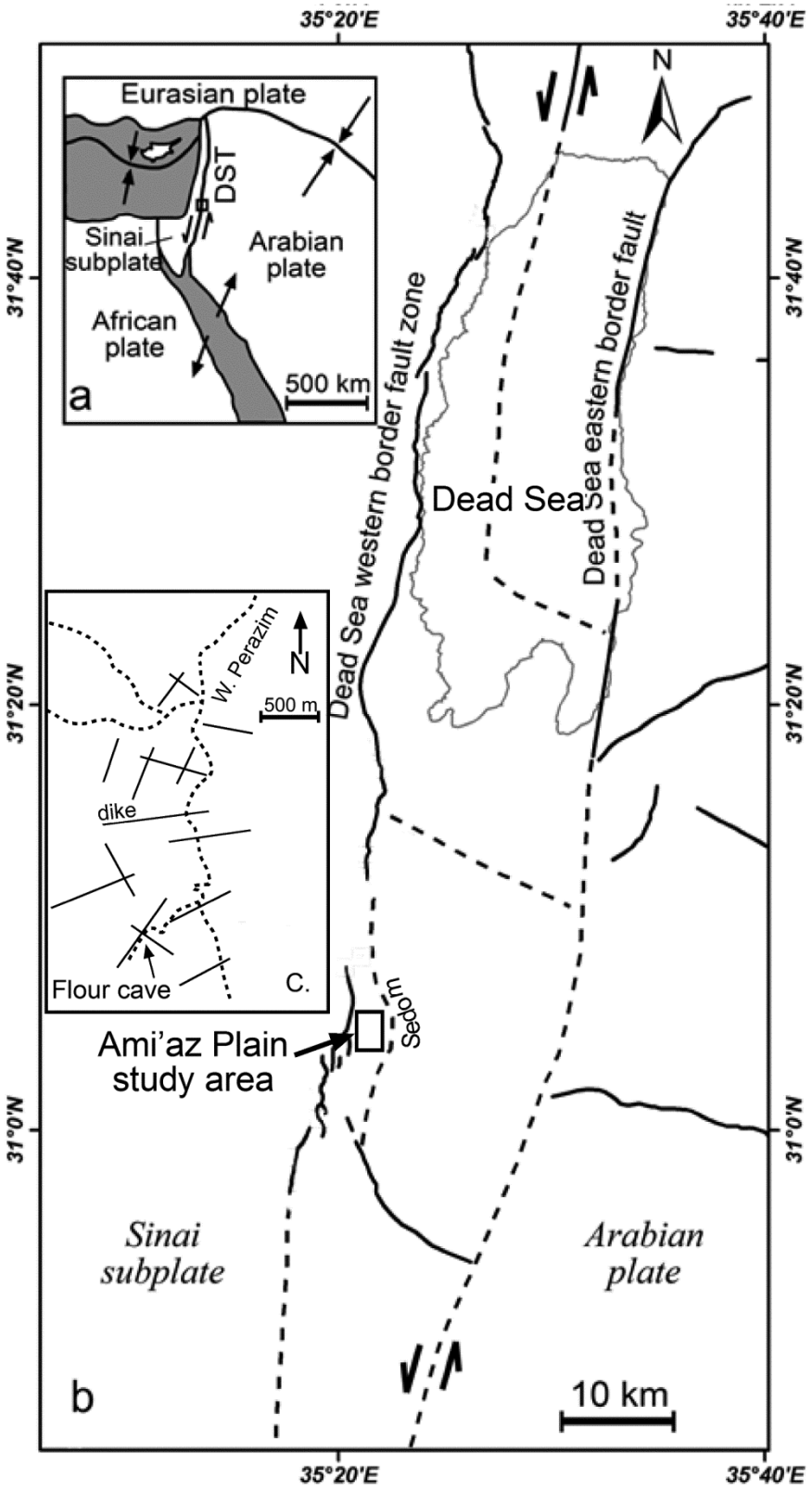

Figure 1

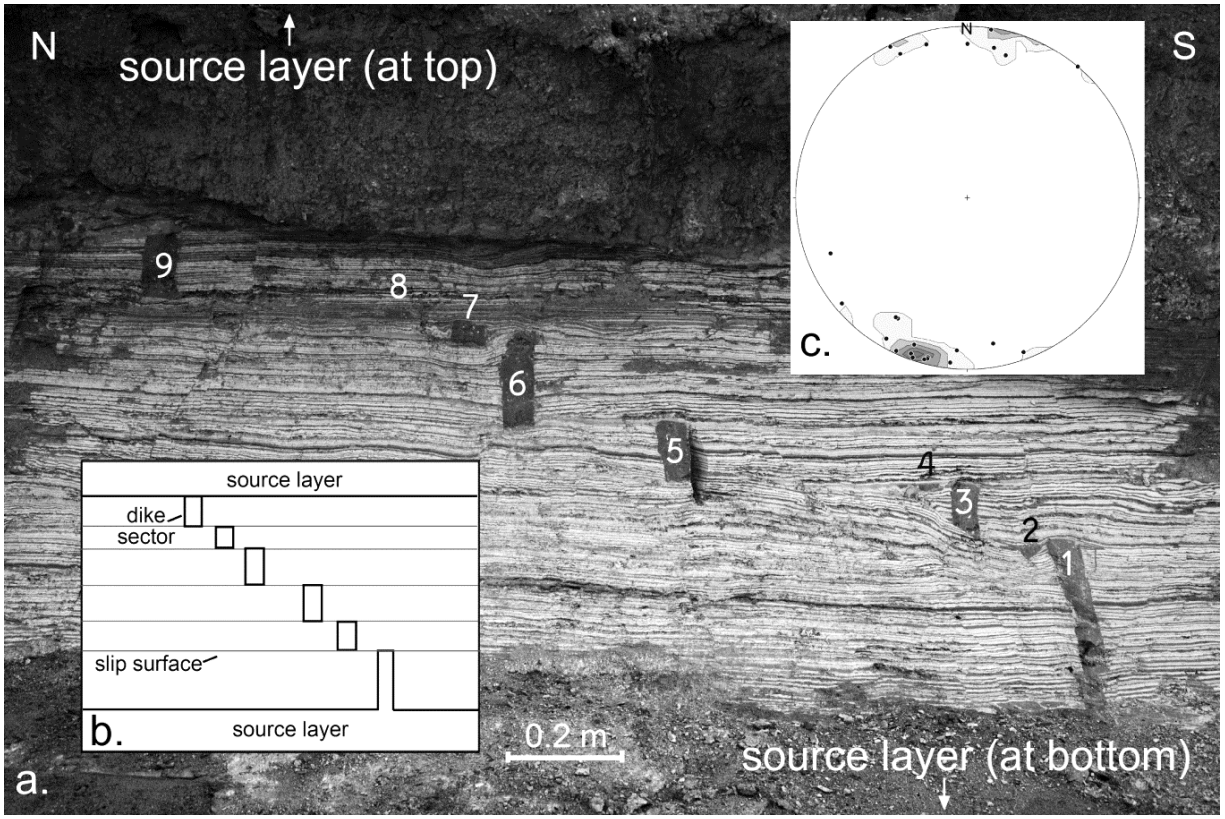
N
source layer (at top)
S
9
8
7
6
5
4
3
2
1
c.
N
source layer
dike
sector
slip surface
b.
source layer
0.2 m
source layer (at bottom)
a.

Figure 2

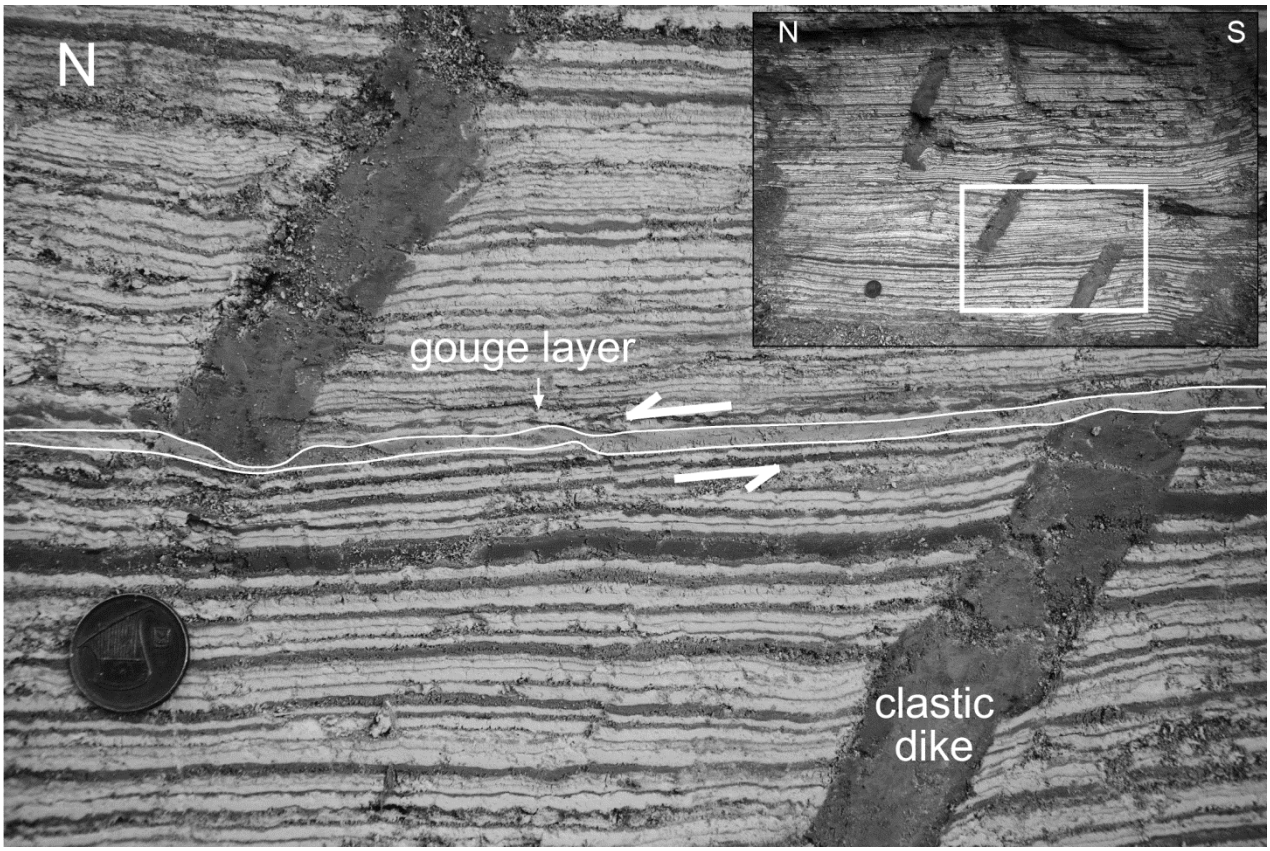

Figure 3

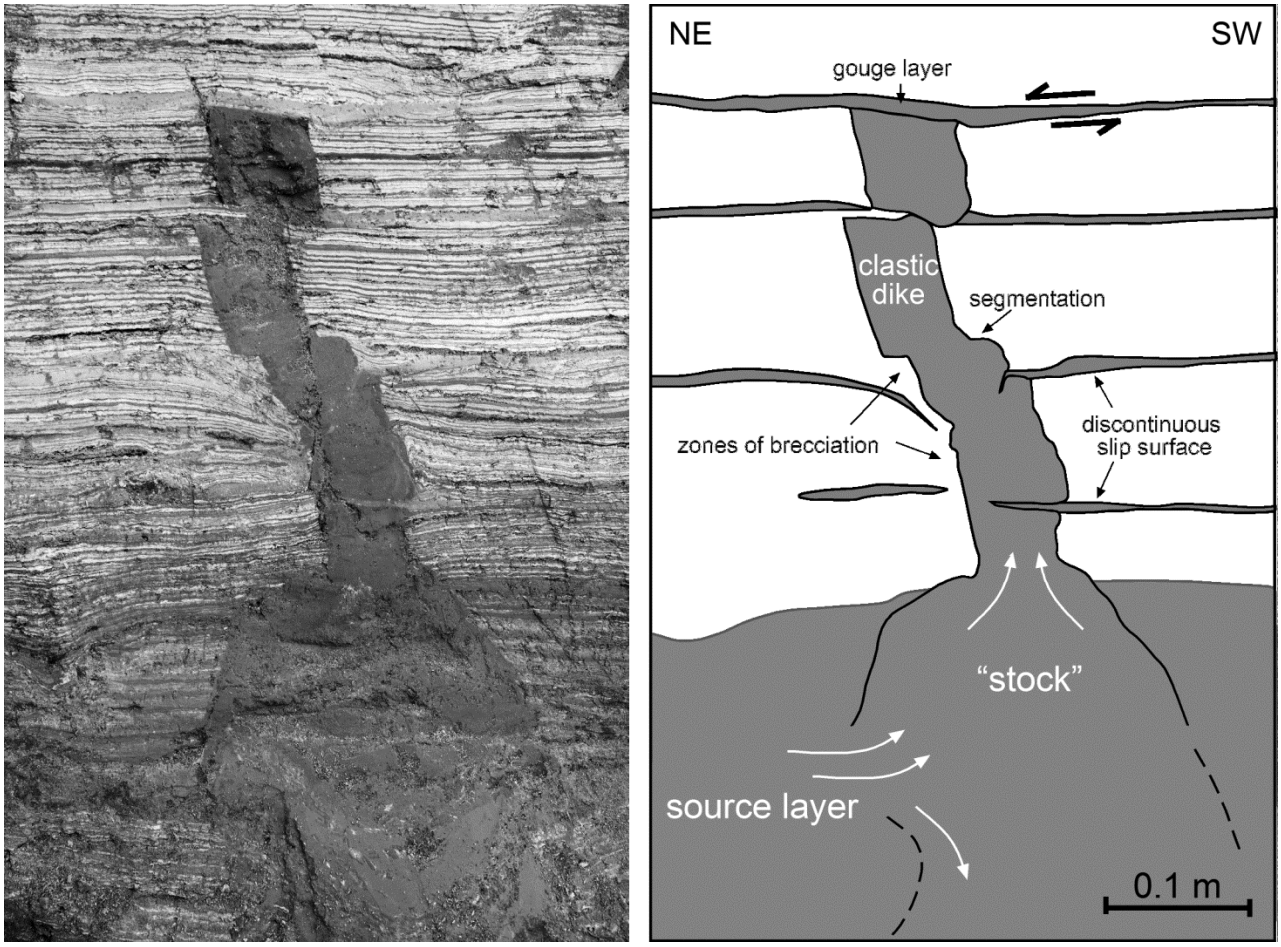
NE
SW
gouge layer
clastic dike
segmentation
zones of brecciation
discontinuous slip surface
"stock"
source layer
0.1 m

Figure 4

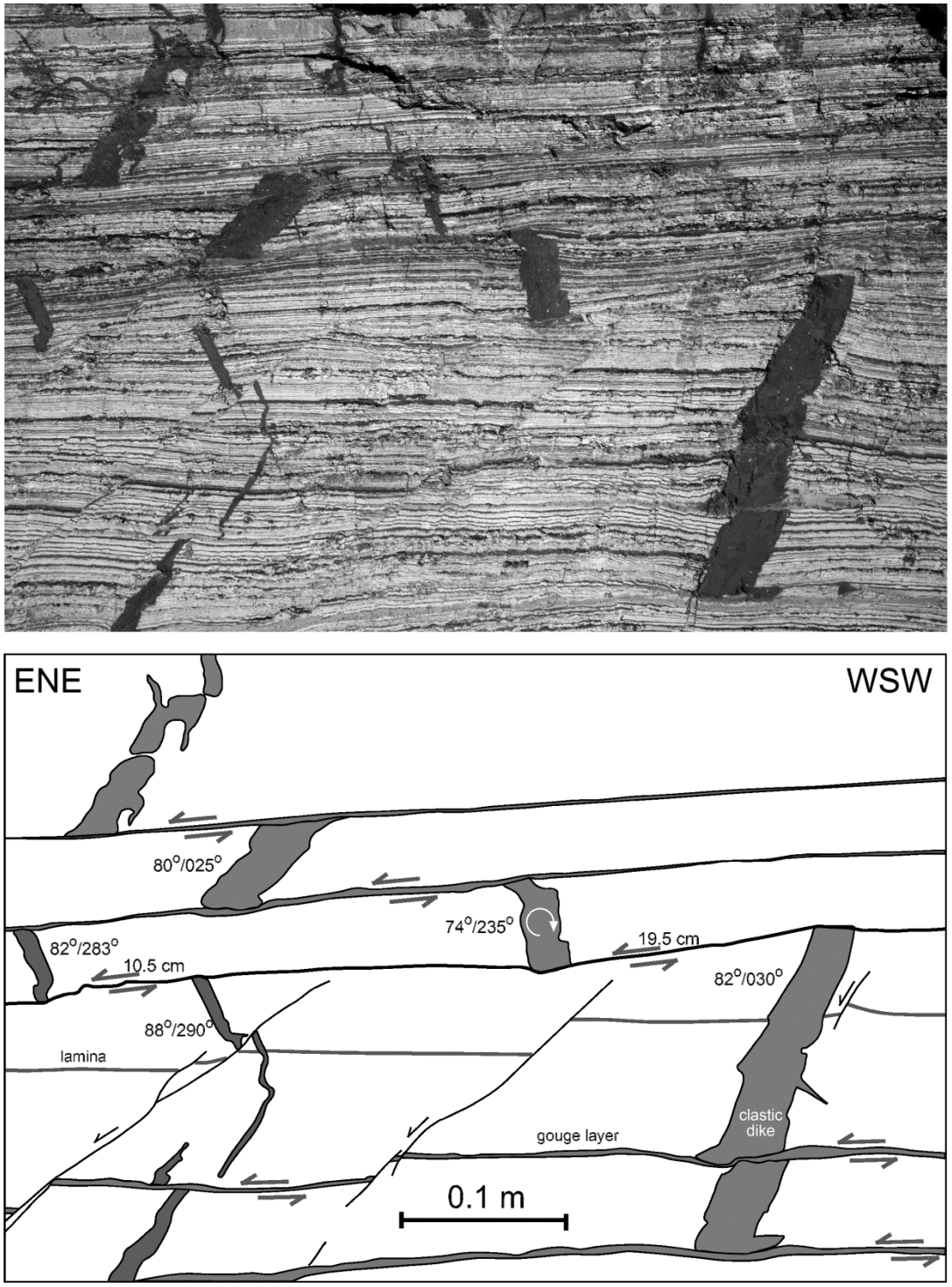
ENE
WSW
80°/025°
74°/235°
82°/283°
10.5 cm
19.5 cm
82°/030°
88°/290°
lamina
gouge layer
clastic dike
0.1 m

Figure 5

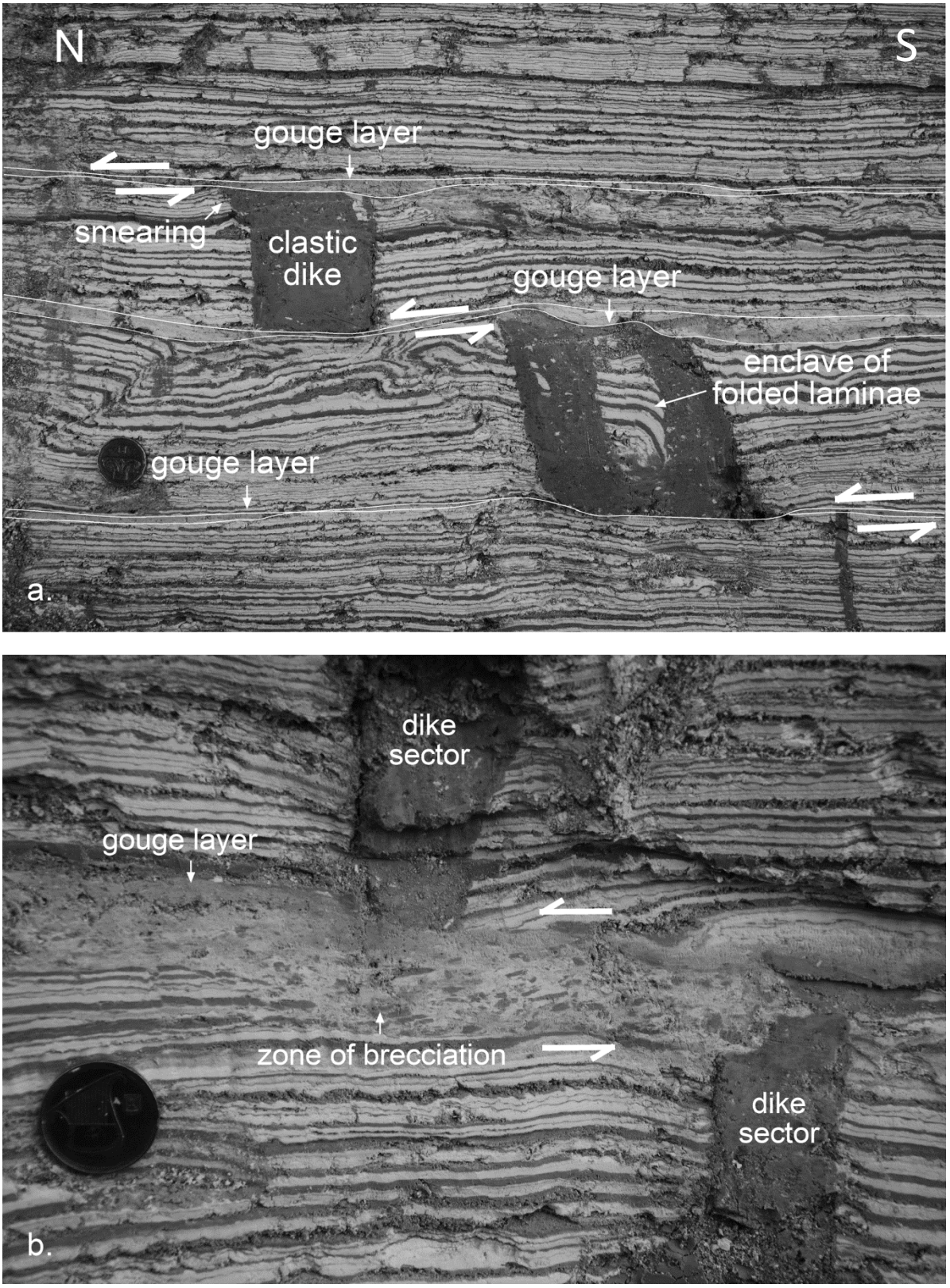
N
S
gouge layer
smearing
clastic dike
gouge layer
enclave of folded laminae
gouge layer
a.
dike sector
gouge layer
zone of brecciation
dike sector
b.

Figure 6

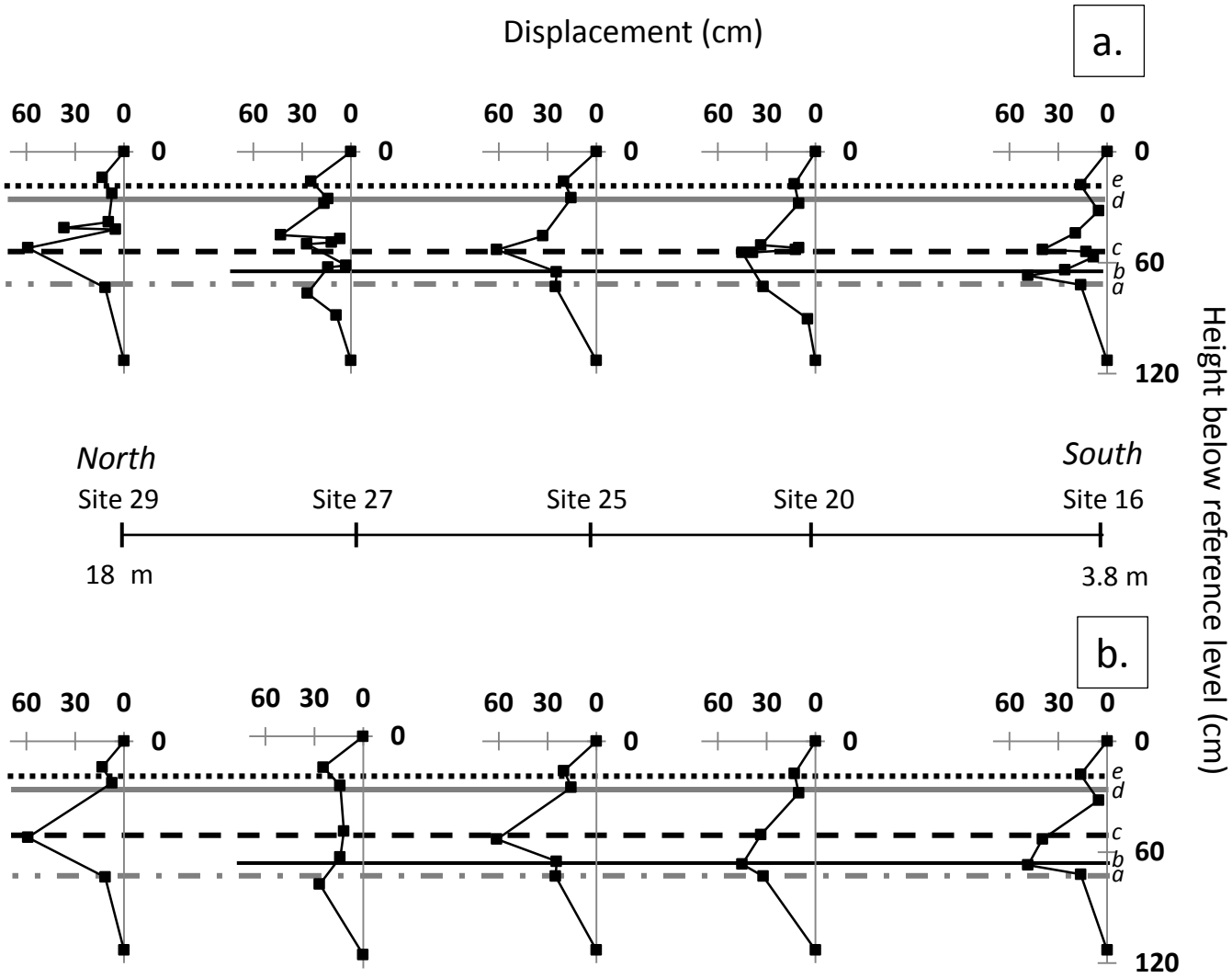
Displacement (cm)
a.
60 30 0
0
e
d
c
b
a
60
120
Height below reference level (cm)
North
South
Site 29
Site 27
Site 25
Site 20
Site 16
18 m
3.8 m
b.

Figure 7

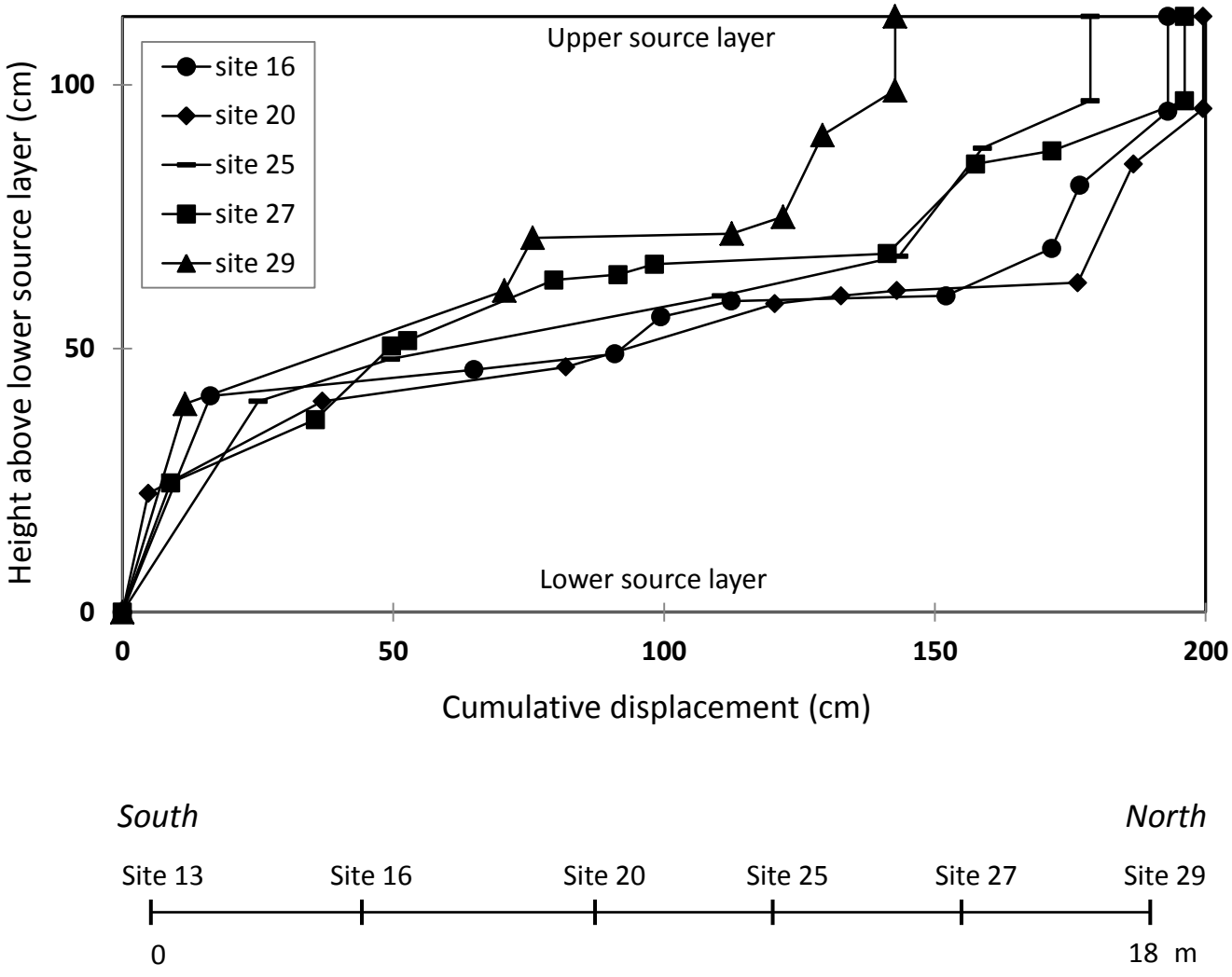
Upper source layer
site 16
site 20
site 25
site 27
site 29
Height above lower source layer (cm)
100
50
0
Lower source layer
0
50
100
150
200
Cumulative displacement (cm)

South
North
Site 13
Site 16
Site 20
Site 25
Site 27
Site 29
0
18 m

Figure 8

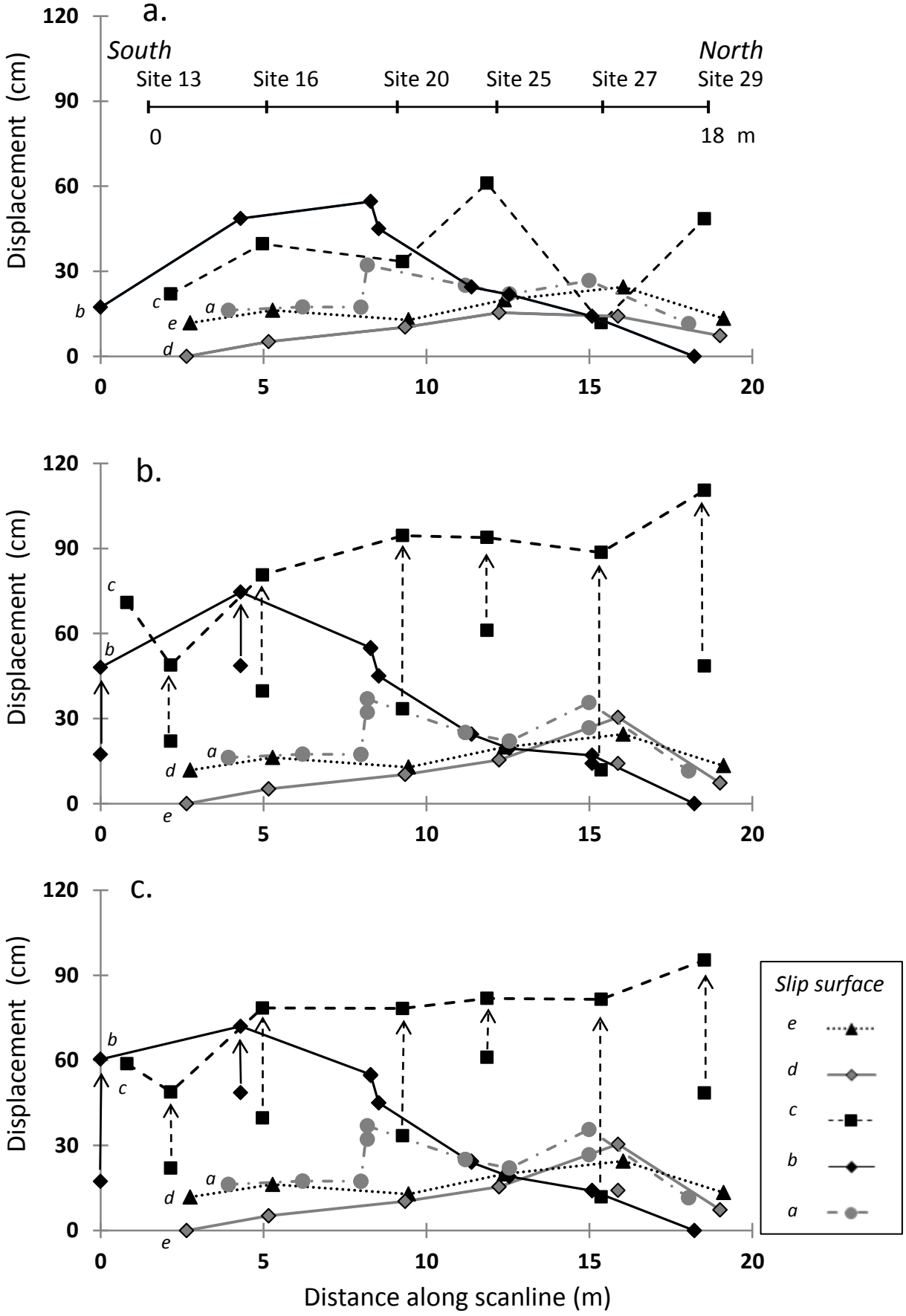
a.
South
North
Site 13
Site 16
Site 20
Site 25
Site 27
Site 29
0
18 m
Displacement (cm)
120
90
60
30
0
0
5
10
15
20
b
a
c
d
e
b.
c
b
a
d
e
C.
b
c
a
d
e
Slip surface
e
d
c
b
a
Distance along scanline (m)

Figure 9

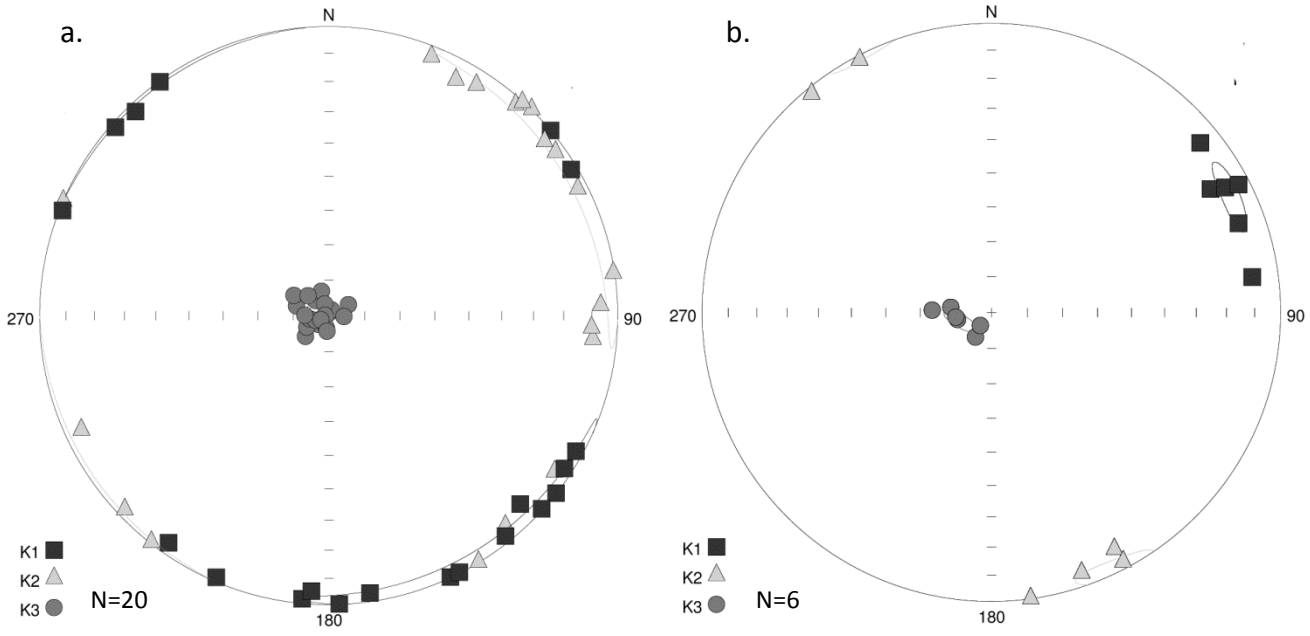

Figure 10

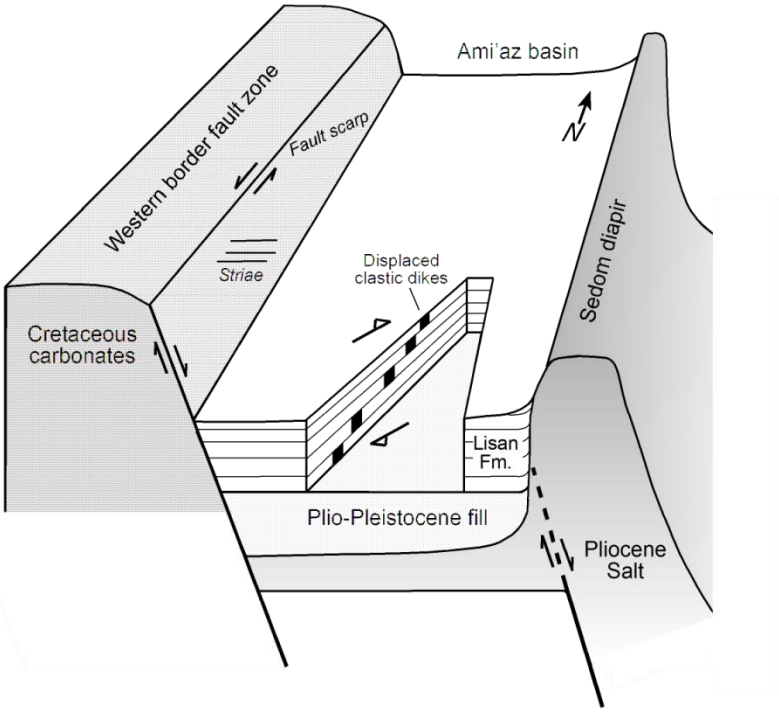
Ami'az basin
Western border fault zone
Fault scarp
Striae
Displaced
clastic dikes
Sedom diapir
Cretaceous
carbonates
Lisan
Fm.
Plio-Pleistocene fill
Pliocene
Salt

Figure 11

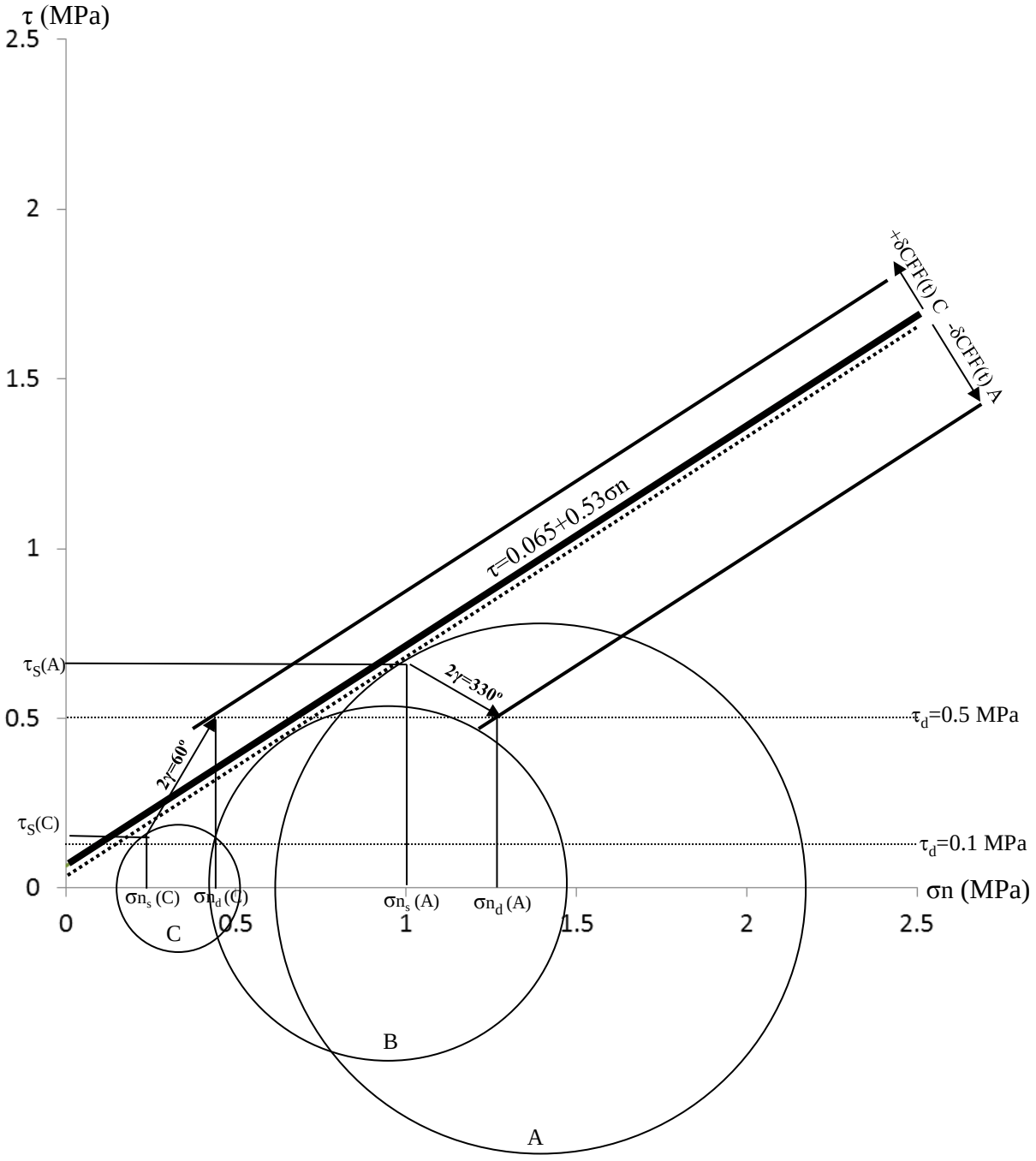
τ (MPa)
2.5
2
1.5
1
0.5
0
τS(A)
τS(C)
τd=0.5 MPa
τd=0.1 MPa
τ=0.065+0.53σn
+δCFF(t) C
-δCFF(t) A
2γ=60°
2γ=330°
σns (C)
σnd (C)
σns (A)
σnd (A)
σn (MPa)
0
0.5
1
1.5
2
2.5
C
B
A

Figure 12

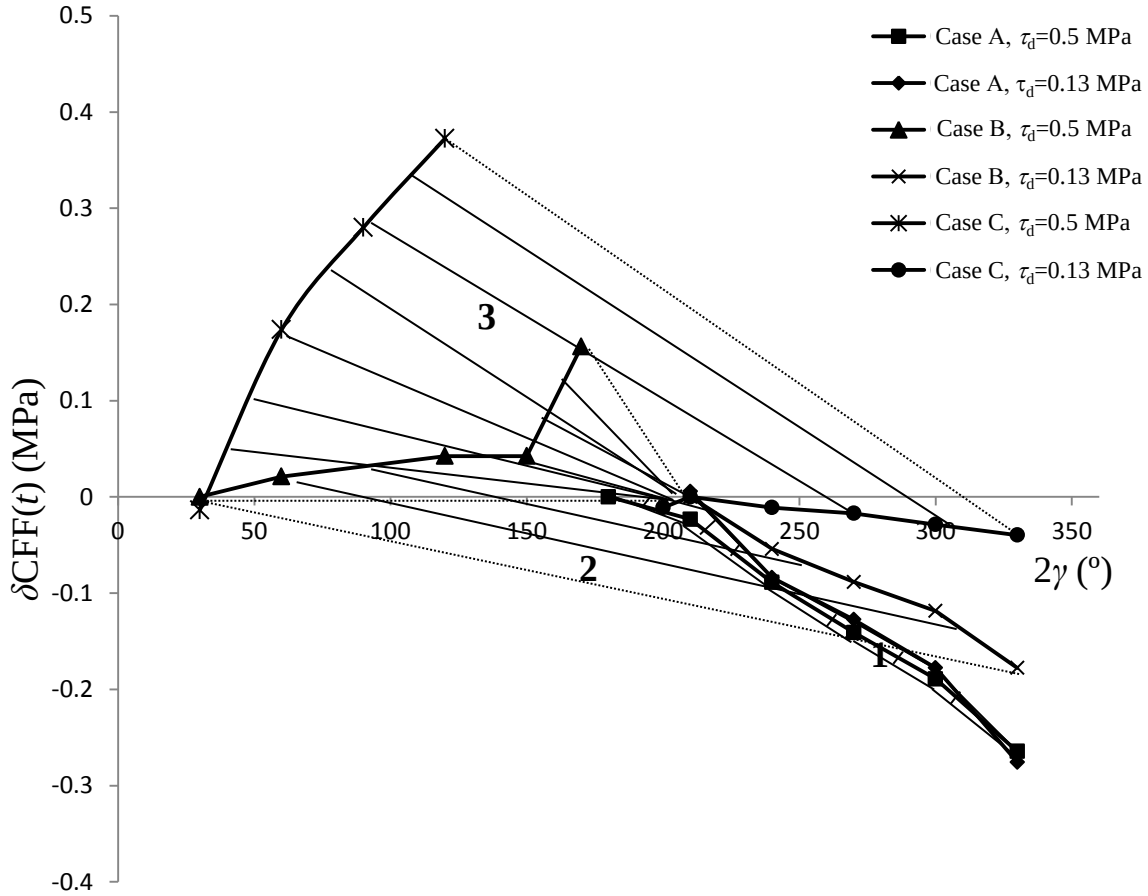
Case A, τ_d=0.5 MPa
Case A, τ_d=0.13 MPa
Case B, τ_d=0.5 MPa
Case B, τ_d=0.13 MPa
Case C, τ_d=0.5 MPa
Case C, τ_d=0.13 MPa
0.5
0.4
0.3
0.2
0.1
0
-0.1
-0.2
-0.3
-0.4
0
50
100
150
200
250
300
350
δCFF(t) (MPa)
2γ (°)
1
2
3

Figure 13

Table

Table 1. Static stress and elastic parameters for geologic settings A-C

Geologic setting	Lake depth (m)	Lisan thickness (m)	Cohesion $C_{o,}$ * (MPa)	Angle of internal friction, Ø*, (°)	Coefficient of internal friction, μ	Density of Lake Lisan, ρ† (kg/m3)	Density of Lisan Fm., ρ*,§ (kg/m3)	Poisson's ratio, υ §	σ_n (MPa)	τ (MPa)	σ_1 (MPa)	σ_3 (MPa)	Shear modulus, G, § (MPa)
A	80	10	0.065	33	0.53	1078	1650	0.4	1.01	0.67	2.16	0.62	100
B	50	10	0.065	33	0.53	1078	1650	0.4	0.69	0.46	1.48	0.43	100
C	0	15	0.065	33	0.53	1078	1650	0.4	0.24	0.16	0.52	0.15	100

* Arkin and Micaheli (1986)

† Starinsky (1974)

§ Levi el al. (2008)